



# Bi-paratopic and multivalent VH domains block ACE2 binding and neutralize SARS-CoV-2

Colton J. Bracken<sup>1</sup>, Shion A. Lim<sup>1</sup>, Paige Solomon<sup>1</sup>, Nicholas J. Rettko<sup>1</sup>, Duy P. Nguyen<sup>1,5</sup>, Beth Shoshana Zha<sup>2</sup>, Kaitlin Schaefer<sup>1</sup>, James R. Byrnes<sup>1</sup>, Jie Zhou<sup>1</sup>, Irene Lui<sup>1</sup>, Jia Liu<sup>1,6</sup>, Katarina Pance<sup>1</sup>, QCRG Structural Biology Consortium\*, Xin X. Zhou<sup>1</sup>, Kevin K. Leung<sup>1</sup> and James A. Wells<sup>1,3,4</sup>✉

**Neutralizing agents against SARS-CoV-2 are urgently needed for the treatment and prophylaxis of COVID-19. Here, we present a strategy to rapidly identify and assemble synthetic human variable heavy (VH) domains toward neutralizing epitopes. We constructed a VH-phage library and targeted the angiotensin-converting enzyme 2 (ACE2) binding interface of the SARS-CoV-2 Spike receptor-binding domain (Spike-RBD). Using a masked selection approach, we identified VH binders to two non-overlapping epitopes and further assembled these into multivalent and bi-paratopic formats. These VH constructs showed increased affinity to Spike (up to 600-fold) and neutralization potency (up to 1,400-fold) on pseudotyped SARS-CoV-2 virus when compared to standalone VH domains. The most potent binder, a trivalent VH, neutralized authentic SARS-CoV-2 with a half-maximal inhibitory concentration ( $IC_{50}$ ) of 4.0 nM (180 ng ml<sup>-1</sup>). A cryo-EM structure of the trivalent VH bound to Spike shows each VH domain engaging an RBD at the ACE2 binding site, confirming our original design strategy.**

The emergence of SARS-CoV-2 and the associated COVID-19 disease has emphasized the need to rapidly generate therapeutics against novel pathogens. SARS-CoV-2 enters cells through the interaction of the viral Spike receptor-binding domain (Spike-RBD) and host angiotensin-converting enzyme-2 (ACE2) on the surface of lung epithelial cells<sup>1</sup>. Antibody and antibody-like biologics that can block this interaction are promising therapeutic candidates because of their high specificity and neutralization potency<sup>2</sup>. The majority of antibodies isolated so far against SARS-CoV-2, SARS-CoV-1 and MERS are derived from screening the B cells of infected patients or repurposed from animal immunizations<sup>3–7</sup>. These approaches, though effective, can be time-consuming and may not necessarily yield neutralizing antibodies. Given the pressing nature of this pandemic, there is a need for multiple parallel strategies to rapidly produce potent, recombinant and neutralizing biologics.

In vitro display technologies using yeast or phage are well-established approaches for generating high-affinity binders from large naive libraries<sup>8</sup>. In vitro selection can be done without infected individuals and only requires the recombinant protein target. One of the recently developed modalities comprises small single-domain antibodies derived from variable heavy homodimer (VHH) domains of antibodies from camels or llamas, often referred to as nanobodies, and are usually obtained by camelid immunization and B-cell cloning<sup>9–12</sup>. Nanobodies have some advantages. Their single chain and small size (11–15 kDa) allow them to bind epitopes or penetrate tissues that may not be accessible to monoclonal antibodies (mAbs; 150 kDa), and nanobodies can be produced rapidly in *Escherichia coli*<sup>13,14</sup>. However, nanobodies derived from animal immunization can also suffer from long turnaround times.

Although this can be overcome with synthetic nanobody libraries<sup>15,16</sup>, nanobody scaffolds that are animal-derived raise significant concerns regarding immunogenicity. More recently, variable heavy (VH) domains derived from human scaffolds have been produced and tested against a number of targets<sup>17–19</sup>.

Accordingly, we and others have been interested in developing VH binders to SARS-CoV-2 for the present pandemic, and as a test case for future ones<sup>6,20–22</sup>. However, one limitation of synthetic single-domain binders is that, as monomers, they often lack the strong binding affinity necessary for therapeutic application. Affinity maturation can improve this, although this extends the development timeline. Instead, generating linked multivalent or multi-paratopic VH binders could be a more rapid approach to utilize avidity to boost affinity and efficacy<sup>23</sup>. Linking VH domains into such homo- and hetero-bifunctional formats is more straightforward than preparing similar multifunctional antibodies, because the latter requires correct heavy- and light-chain pairing to maintain binding affinity, whereas multifunctional VH domains have no such requirements<sup>11</sup>.

Here, we construct a human VH-phage library derived from the clinically approved trastuzumab scaffold and validate its use on multiple antigens. By utilizing a masked phage selection strategy, we rapidly identify VH domains at two non-overlapping epitopes within the ACE2 binding site of the SARS-CoV-2 Spike-RBD. By linking these VH domains with a strategic linker into bi-paratopic and multivalent binders, we improve the affinity from mid-nanomolar to ~100 pM, without any additional high-resolution structural information. These high-affinity binders are capable of potently neutralizing pseudotyped and live SARS-CoV-2. A cryo-EM structure of the most potent trivalent VH bound to Spike shows that each VH domain

<sup>1</sup>Department of Pharmaceutical Chemistry, University of California, San Francisco, San Francisco, CA, USA. <sup>2</sup>Department of Pulmonary, Critical Care, Allergy and Sleep Medicine, University of California San Francisco, San Francisco, CA, USA. <sup>3</sup>Department of Cellular & Molecular Pharmacology, University of California San Francisco, San Francisco, CA, USA. <sup>4</sup>Chan Zuckerberg Biohub, San Francisco, CA, USA. <sup>5</sup>Present address: Lyell Immunopharma Inc., Seattle, WA, USA. <sup>6</sup>Present address: Merck & Co., South San Francisco, CA, USA. \*A list of authors and their affiliations appears at the end of the paper. ✉e-mail: [jim.wells@ucsf.edu](mailto:jim.wells@ucsf.edu)

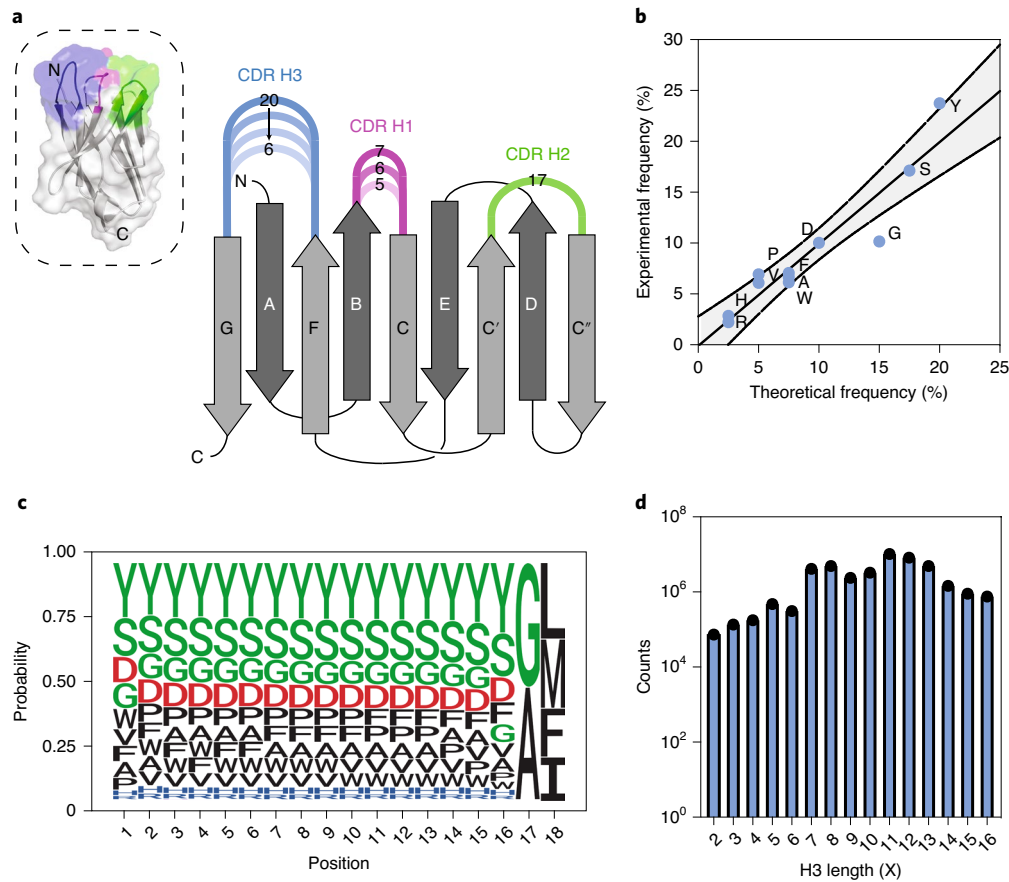


**Fig. 1 | Design and validation of the VH-phage library.** **a**, Three-dimensional (3D) surface representation (left) of the VH-4D5 parental scaffold (PDB 1FVC) and a cartoon diagram (right), where individual CDRs are annotated in color with the designed loop length variations according to the Kabat nomenclature<sup>31</sup>. **b**, NGS analysis of the longest H3 loop ( $X=16$ ), showing that the expected global amino-acid frequencies are comparable to the designed frequencies. The gray shaded region denotes the 95% confidence interval. **c**, Representative NGS analysis of the longest H3 loop ( $X=16$ ), showing that the positional frequency distribution matches the designed frequencies. Position 1 refers to residue 95 (Kabat definition). Data for the other CDR H3 lengths are reported in Supplementary Fig. 2. **d**, NGS analysis of unique clones, showing that all H3 lengths are represented in the pooled VH-phage library.

precisely targets the ACE2 binding interface on all three RBDs of Spike. We believe our VH-phage library and this multivalent and multi-paratopic approach is highly advantageous in targeting distinct epitopes within an antigen and can be broadly applied to other viral and non-viral targets to leverage avidity for increased potency.

## Results

**Construction of a synthetic human VH-phage library.** To enable the generation of single-domain antibodies against targets such as SARS-CoV-2 Spike, we designed a synthetic VH-phage library using the VH domain (4D5) from the highly stable and clinically successful trastuzumab antibody (Fig. 1a)<sup>24,25</sup>. The VH scaffold was modified to include five amino-acid changes predicted to reduce aggregation (Supplementary Table 1)<sup>26</sup>. To bias toward colloidal stability, aspartate and arginine or glutamate residues were inserted at the beginning and at two or three terminal positions of the complementarity-determining region (CDR) H1, as these have been used previously to improve the aggregation resistance of VH and scFv fragments from the VH3 germline<sup>19,27</sup>. Diversity was introduced into CDR H1 and CDR H2 using a minimalistic approach, where variability was largely restricted to tyrosine and serine residues (Extended Data Fig. 1)<sup>28</sup>. We introduced high-diversity mixtures of amino acids into CDR H3 because it is usually critical to antigen recognition (Extended Data Fig. 1), and Fab-phage libraries with highly diverse CDR H3 sequences have successfully

yielded high-affinity antibodies to a variety of target antigens<sup>29,30</sup>. Furthermore, charged polar residues such as aspartate were introduced at 10% frequency to decrease the net surface hydrophobicity to mitigate aggregation and decrease the propensity for non-specific binders in the library.

Based on previous designs, we chose loop length variations of 5–7 residues in CDR H1 and 6–20 residues in CDR H3, while CDR H2 was kept constant at 17 residues (Kabat definitions; Extended Data Fig. 1 and Supplementary Table 2)<sup>29,31</sup>. To cover this large sequence space with a minimal bias towards different length variants, five separate sub-libraries were constructed by binning CDR H3 loop length insertions ( $X_{2-16}$ ) in incremental sets of three and combined to yield a final library of  $\sim 5 \times 10^{10}$  transformants (Supplementary Fig. 1). Analysis of the unique CDR H3 sequences by next-generation sequencing (NGS) showed that the observed amino-acid frequencies closely matched our designs and all CDR H3 length variants were represented in the final library (Fig. 1b–d and Supplementary Fig. 2). Finally, to test the performance of the library, several rounds of panning were performed on representative antigens including both cytosolic and membrane proteins. These panning experiments were done in parallel with an in-house Fab-phage library. For all target antigens, high levels of enrichment were observed (Supplementary Fig. 3). For the majority of antigens, enrichment levels were comparable or substantially higher for the VH-phage library than for the Fab-phage library.

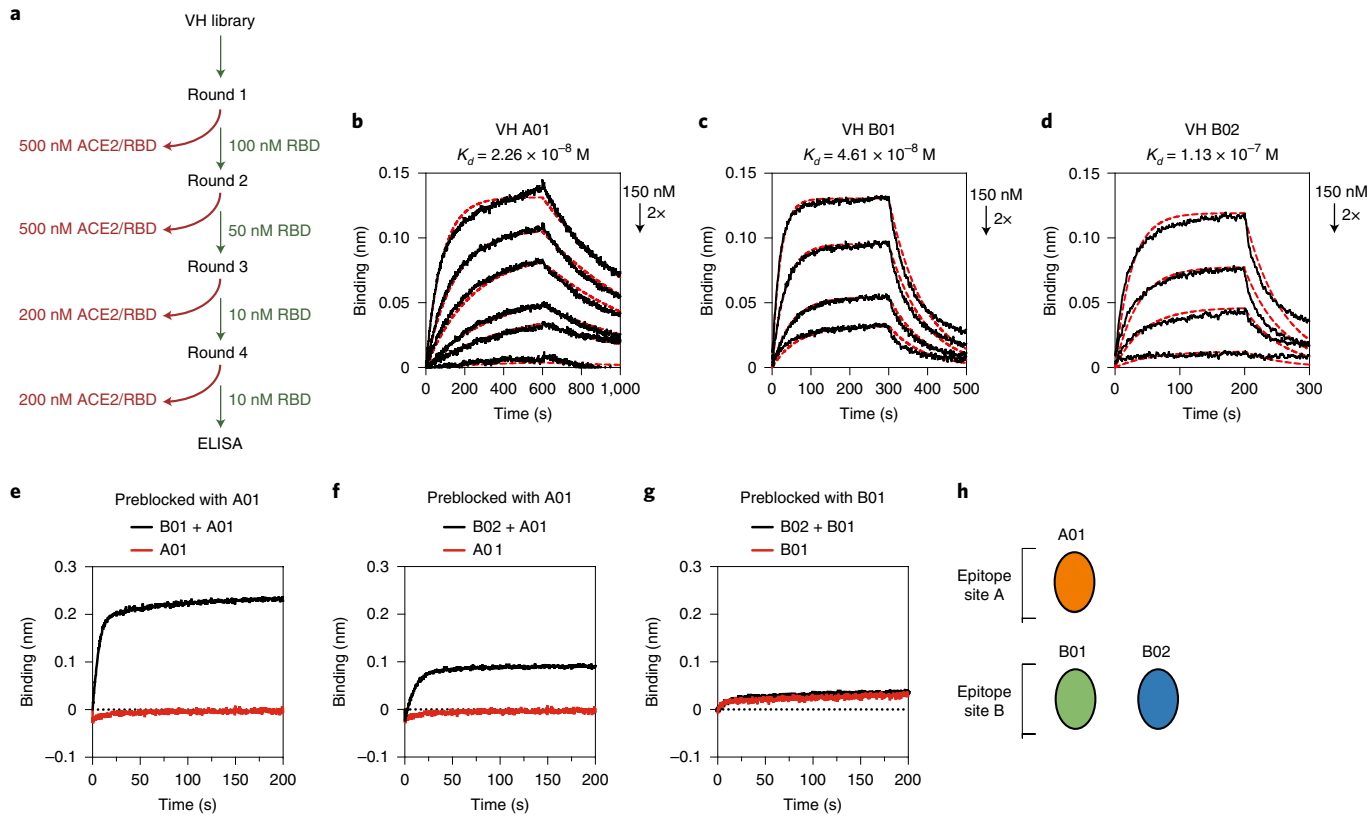


**Fig. 2 | Identification of VH domains that bind Spike-RBD at two unique epitopes by phage display.** **a**, Diagram illustrating the phage selection strategy to isolate VH-phage that bind at the ACE2 binding interface. Red indicates clearance of the phage pool by the Spike-RBD-Fc/ACE2-Fc complex; green indicates positive selection against Spike-RBD-Fc alone. To increase stringency, successively lower concentrations of Spike-RBD-Fc were used and, after four rounds of selection, individual phage clones were analyzed by phage ELISA. **b-d**, Bio-layer interferometry (BLI) of VH A01 (**b**), VH B01 (**c**) and VH B02 (**d**) against Spike-RBD. **e-g**, BLI-based epitope binning of VH A01 and VH B01 (**e**), VH A01 and VH B02 (**f**) and VH B01 and VH B02 (**g**). The antigen loaded onto the sensor tip was Spike-RBD. **h**, Diagram of the two different epitope bins targeted by VH domains.

**Identification of VHs that target multiple epitopes.** So far, most neutralizing mAbs against SARS-CoV-2 target Spike and, not surprisingly, many of the most potent target the ACE2 binding interface<sup>3,7</sup>. Although cryo-EM structures show that the ACE2 binding interface remains largely solvent-accessible in both the RBD ‘up’ and ‘down’ conformations<sup>32</sup>, simultaneous intra-molecular engagement by both binding arms of mAbs may be challenging as they are not geometrically arranged to engage multiple RBDs on a single Spike trimer. Thus, our goal was to target this highly neutralizing epitope with VHs and subsequently link them together to utilize avidity beyond that of a homo-bivalent mAb.

We first expressed the Spike-RBD (residues 328–533) and the ACE2 peptidase domain (residues 1–640) as biotinylated Fc-fusions for VH-phage selections<sup>33</sup>. To specifically enrich for VH-phage that bind the ACE2 binding site on Spike-RBD, the library was first cleared with the Spike-RBD-Fc/ACE2-Fc complex to remove phage that bound outside the ACE2 binding interface. This was followed by selection on Spike-RBD-Fc alone to enrich for phage that bound the unmasked ACE2 binding site (Fig. 2a). By rounds 3 and 4, significant enrichments for phage that bound Spike-RBD-Fc but not the Spike-RBD-Fc/ACE2-Fc complex were observed (Supplementary Fig. 4a). Single clones were isolated and characterized for their ability to bind Spike-RBD-Fc by phage enzyme-linked immunosorbent assays (ELISAs; Supplementary Fig. 4b). Nearly all VH-phage showed enhanced binding to Spike-RBD-Fc over the Spike-RBD-Fc/ACE2-Fc complex, suggesting they bound the same epitope as ACE2 and could potentially block this interaction

(Supplementary Fig. 4c). In total, 85 unique VH-phage sequences were identified, and a subset was characterized as recombinant VH domains. We identified three lead VH candidates that bound Spike-RBD with  $K_d$  values ranging from 23 to 113 nM (Fig. 2b–d). These VH were specific to Spike-RBD and did not recognize other in-house antigens (Extended Data Fig. 2). Epitope binning demonstrated that the three VH domains mapped to two non-overlapping epitopes (which we call site A and site B) within the larger ACE2 binding site (Supplementary Fig. 5). The VH domain that recognizes site A (A01) binds independently from the VHs that recognize site B (B01 and B02) (Fig. 2e–h).

**Bi-paratopic and multivalent linkage increases affinity.** We chose two parallel approaches to increase the affinity of the VH binders to Spike through avidity. First, we reasoned that VHs targeting site A or site B are in close proximity because they are non-overlapping but compete for the larger ACE2 binding site. Therefore, these VHs could be linked together to engage the same RBD simultaneously and improve affinity through intra-RBD avidity. Using the three VH monomers (A01, B01, B02) as modular units, we generated two bi-paratopic linked dimers ( $\text{VH}_2$ ) by fusing A01 with B01 or B02 (Fig. 3a). In a parallel approach, we aimed to leverage the trimeric nature of Spike and engage multiple RBDs on the same Spike simultaneously to improve affinity through inter-RBD avidity. To that end, we generated mono-paratopic Fc fusions ( $\text{VH}-\text{Fc}$ ), linked dimers ( $\text{VH}_2$ ) and linked trimers ( $\text{VH}_3$ ) (Fig. 3a). The  $\text{VH}_2$  and  $\text{VH}_3$  consisted of a C-to-N terminal fusion of two or three VH monomers via

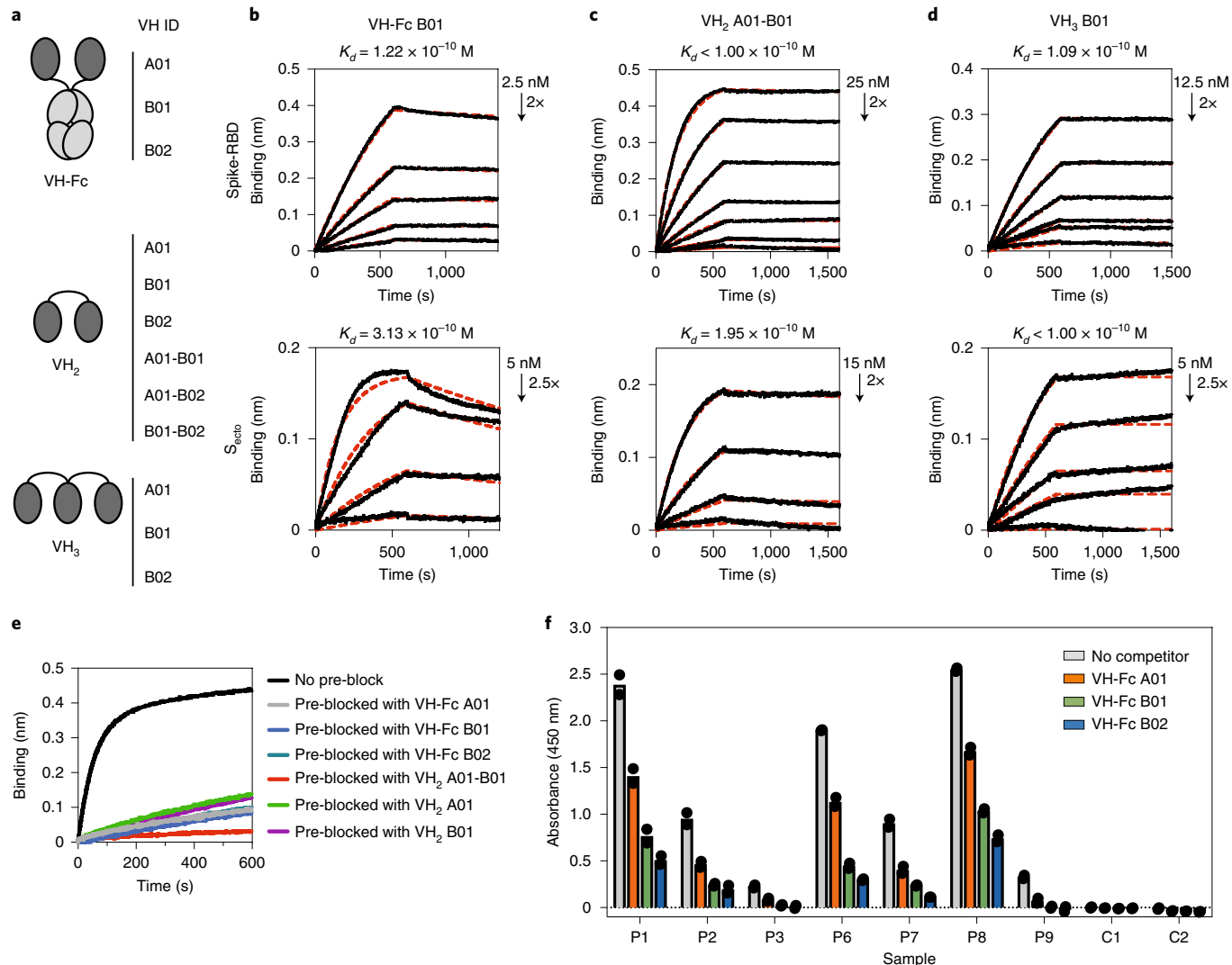


**Fig. 3 | In vitro characterization of multivalent and bi-paratopic VH binders.** **a**, Cartoon depiction of engineered VH binders generated by linking VH domains via Fc-fusion or a 20-amino-acid Gly-Ser linker (~70 Å), while the VH-Fc consisted of a fusion of VH to the human IgG1 Fc domain via a flexible Fc hinge (~100 Å). The structure of the SARS-CoV-2 Spike trimer suggests that the linked VH domains could bridge the distance between RBDs on an individual Spike (<55 Å), but are unlikely to span RBDs between discrete Spike proteins based on the inter-Spike distance on the viral envelope (150–180 Å) (Extended Data Fig. 3)<sup>32,34</sup>. **b–d**, BLI traces of lead VH binders VH-Fc B01 (**b**), VH<sub>2</sub> A01-B01 (**c**) and VH<sub>3</sub> B01 (**d**) against RBD (upper panel) or S<sub>ecto</sub> (lower panel). **e**, Sequential BLI binding experiments measuring binding of ACE2-Fc to S<sub>ecto</sub> pre-blocked with our VH binders, showing that multivalent VH binders can block ACE2-Fc binding to S<sub>ecto</sub>. **f**, Competition serology ELISA with convalescent patient sera, showing that VH-Fc binders can compete with patient antibodies. P1 to P9 represent sera from individuals with a history of previous SARS-CoV-2 infection. C1 and C2 are sera collected from two donors before the SARS-CoV-2 outbreak. Individual data points represent technical replicates ( $n=2$ ) from the serum of the same individual and are shown as black circles.

a 20-amino-acid Gly-Ser linker (~70 Å), while the VH-Fc consisted of a fusion of VH to the human IgG1 Fc domain via a flexible Fc hinge (~100 Å). The structure of the SARS-CoV-2 Spike trimer suggests that the linked VH domains could bridge the distance between RBDs on an individual Spike (<55 Å), but are unlikely to span RBDs between discrete Spike proteins based on the inter-Spike distance on the viral envelope (150–180 Å) (Extended Data Fig. 3)<sup>32,34</sup>.

ELISA and bio-layer interferometry (BLI) binding assays to Spike-RBD show that VH-Fc, VH<sub>2</sub> and VH<sub>3</sub> have 2.7- to 600-fold higher affinity to Spike-RBD ( $K_d=0.1\text{--}8.4 \text{ nM}$ ) than the standalone VH monomers (Fig. 3b–d, Extended Data Fig. 4, Supplementary Tables 3 and 4, and Supplementary Fig. 6). Interestingly, fold increases in affinity were greater for binders that target site B or both site A and site B combined. The most potent constructs bound trimeric Spike ectodomain (S<sub>ecto</sub>) with  $K_d$  values in the hundreds of picomolar range, and all utilized VH B01 (Fig. 3b–d). Next, we examined whether these multivalent VH can block ACE2 bind-

ing to Spike by testing several high-affinity constructs (VH-Fcs; VH<sub>2</sub> A01-B01, VH<sub>2</sub> A01 and VH<sub>2</sub> B02) in a sequential BLI binding assay. S<sub>ecto</sub> was immobilized on the biosensor, pre-blocked with each VH binder, and then assayed for binding to ACE2-Fc (Fig. 3e). We found that all tested binders substantially blocked binding of ACE2-Fc to S<sub>ecto</sub>. Similarly, we examined whether these engineered VH-Fcs can compete with SARS-CoV-2 Spike-reactive antibodies in convalescent patient serum. Using a competition ELISA format previously developed by our group<sup>35</sup>, we found that VH-Fcs reduced the binding of patient antibodies to SARS-CoV-2 Spike-RBD (Fig. 3f). Taken together, these data show that modular reformatting of these VH domains can significantly increase the affinity to Spike and block the same immunogenic epitopes as patient-derived Abs.

Finally, we characterized the biophysical properties of these engineered VH by differential scanning fluorimetry (DSF), size exclusion chromatography (SEC) and reconstitution after lyophilization. The VH binders can be expressed in *E. coli* in high yields (VH<sub>2</sub>

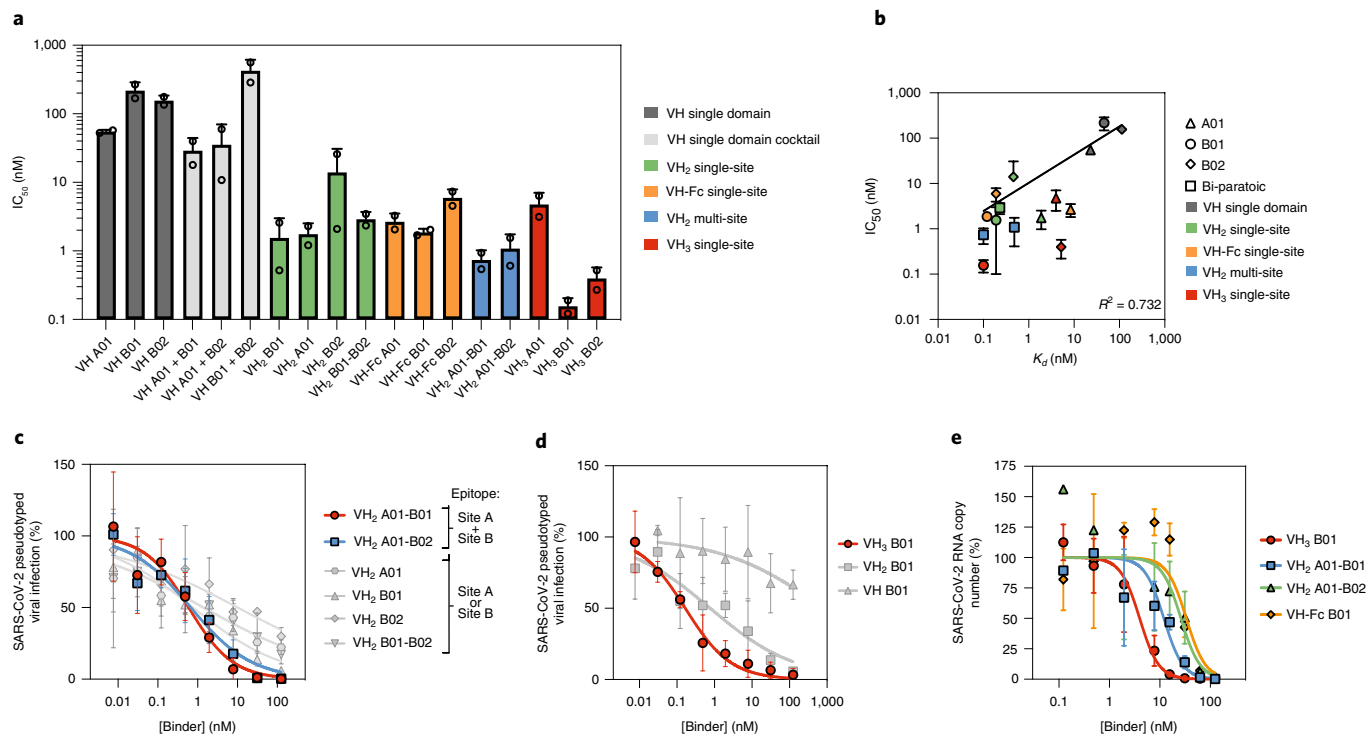


**Fig. 4 | Multivalent and bi-paratopic VH binders neutralize pseudotyped and authentic SARS-CoV-2.** **a**, Pseudotyped virus IC<sub>50</sub> values of VH binders. The neutralization potency improves when VH domains are engineered into multivalent and bi-paratopic constructs. **b**, Correlation of in vitro binding affinity ( $K_d$ ) and pseudotyped virus neutralization (IC<sub>50</sub>) of VH binders. Data were fit to a log-log linear extrapolation. **c**, Pseudotyped virus neutralization curves of multi-site VH<sub>2</sub> in comparison to single-site VH<sub>2</sub> demonstrate that the multi-site VH<sub>2</sub> have a more cooperative neutralization curve. **d**, Pseudotyped virus neutralization curves of mono-, bi- and trivalent formats of VH B01, demonstrating the potency gains driven by valency. **e**, Authentic SARS-CoV-2 neutralization curves for the most potent VH formats were determined via quantitative polymerase chain reaction (qPCR) of the viral genome in cellular RNA. All pseudoviral neutralization data were repeated as  $n=2$  independent replicates. Authentic virus neutralization data were repeated as  $n=2$  independent replicates. Data represent the average and standard deviation of replicates.

A01-B01 and VH<sub>3</sub> B01 express at  $\sim 1 \text{ g l}^{-1}$  in shake flask culture) and have good stabilities (melting temperature ( $T_m$ ) = 56–65 °C) (Supplementary Fig. 7). The most potent binders elute as a single monodisperse peak via SEC (Supplementary Fig. 8), and VH<sub>3</sub> B01 retains binding to Spike-RBD and a monodisperse SEC profile after lyophilization and reconstitution, suggesting it could be suitable for lyophilized formulation (Supplementary Fig. 9).

**Bi-paratopic and multivalent VH neutralize virus.** SARS-CoV2 is a biosafety level 3 (BSL3) pathogen. To facilitate studies under routine laboratory conditions, we utilized a pseudotyped lentiviral (HIV) particle that has been reported previously<sup>36</sup>. These pseudotyped particles were generated from a three-plasmid system containing non-Env proteins from HIV, a luciferase reporter and the SARS-CoV-2 Spike protein. Entry of this viral particle into ACE2-expressing target cells and neutralization by anti-Spike antibodies have previously been shown to faithfully recapitulate features of the authentic pathogen without the need for working under BSL3 conditions. This pseudotyped virus was used to determine the half-maximal inhibitory concentration (IC<sub>50</sub>) of neutralization for each construct.

The VH monomers neutralized pseudotyped virus weakly (IC<sub>50</sub> > 50 nM), and cocktails of unlinked monomers did not improve potency. By contrast, the multivalent binders (VH<sub>2</sub>, VH<sub>3</sub> and VH-Fc) neutralized ~10–1,000-fold more potently than their respective monomeric units (Fig. 4a, Supplementary Table 5 and Extended Data Fig. 5). There was a linear correlation between the in vitro binding affinity ( $K_d$ ) to Spike-RBD and the pseudo-

typed neutralization potency (IC<sub>50</sub>) across the different binders ( $R^2 = 0.72$ ) (Fig. 4b).

In particular, we observed that bi-paratopic VH<sub>2</sub> A01-B01 and VH<sub>2</sub> A01-B02 were stronger neutralizers than unlinked monomer cocktails. Additionally, the neutralization curves of the bi-paratopic (multi-site) VH<sub>2</sub> differed from the homodimeric (single-site) VH<sub>2</sub> binding to either site A or B. That is, the bi-paratopic VH<sub>2</sub> exhibited a more cooperative transition and fully neutralized virus, while the homodimeric VH<sub>2</sub> showed a more linear transition and did not fully block viral entry, even at high concentrations (Fig. 4c). This may reflect mechanistic differences—the bi-paratopic VH<sub>2</sub> can theoretically engage a single RBD using both VH domains simultaneously (intra-RBD avidity) and more fully occlude the ACE2 binding site, while the homodimeric VH<sub>2</sub> must bridge separate RBDs within the trimer (inter-RBD avidity).

Furthermore, the increase in neutralization potency as we increase the number of tandem VH units is exemplified by the VH B01-derived binders, as the IC<sub>50</sub> values of VH<sub>2</sub> B01 and VH<sub>3</sub> B01 are two to three orders of magnitude lower than the IC<sub>50</sub> of the VH B01 monomer (Fig. 4d). This is also observed for VH-Fc B01, which also neutralizes two orders of magnitude more potently than the monomer. Interestingly, although the neutralization potency of VH<sub>2</sub> A01 is better than VH A01, the potency does not improve further when a third domain is added (VH<sub>3</sub> A01), indicating that epitope-specific geometries can affect the extent to which increasing valency improves potency. The pseudotyped virus neutralization assays demonstrate that the top predicted binders from in vitro affinity data, VH<sub>2</sub> A01-B01, VH<sub>2</sub> A01-B02, VH<sub>3</sub> B01 and

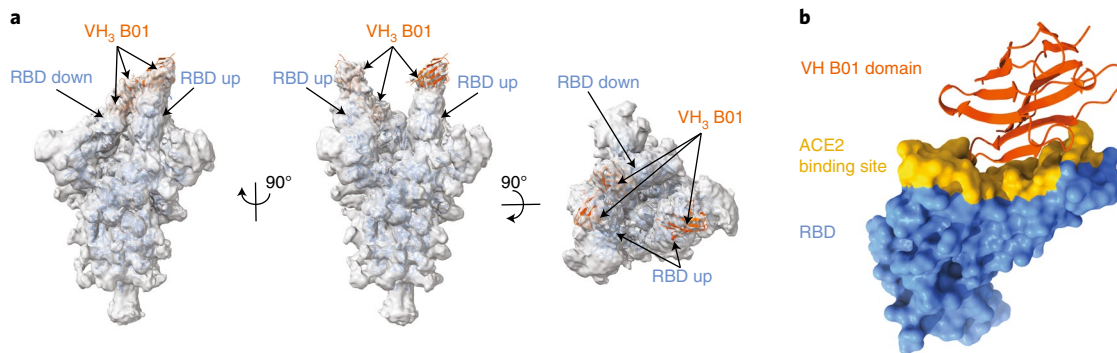


**Fig. 5 | Cryo-EM reveals trivalent VH binding at the ACE2 binding interface of RBD.** **a**, Side and top views of cryo-EM 3D reconstructions of  $\text{VH}_3$  B01 +  $S_{\text{ecto}}$  (PDB 7JWB), shown with individual VH domain densities of  $\text{VH}_3$  B01 fit with PDB 3P9W (VH scaffold; orange cartoon). A total of three VH domains, each bound to an RBD of the Spike trimer, are resolved. The 3D model of  $S_{\text{ecto}}$  was fit with a reference structure (PDB 6X2B, with additional rigid body fit of the individual RBDs; blue cartoon) and shows RBDs in a distinct two ‘up’, one ‘down’ conformation. The cryo-EM map was low-pass-filtered to 6 Å. **b**, View of the epitope (site B) of one VH domain from  $\text{VH}_3$  B01. Site B overlays directly with the ACE2 binding site (yellow surface; contacts defined as RBD residues within 8 Å of an ACE2 residue from PDB 6MOJ).

VH-Fc B01, are indeed the most potent, with  $\text{IC}_{50}$  values of 0.74 nM, 1.08 nM, 0.156 nM and 1.86 nM, respectively.

Finally, we tested the ability of the most potent VH binders to neutralize authentic SARS-CoV-2 virus. As predicted,  $\text{VH}_3$ -B01 neutralized most potently. The VH-Fc B01,  $\text{VH}_2$  A01-B01 and  $\text{VH}_2$  A01-B02 followed trends consistent with both the *in vitro* binding  $K_d$  and pseudotyped virus  $\text{IC}_{50}$ .  $\text{VH}_3$  B01, VH-Fc B01,  $\text{VH}_2$  A01-B01 and  $\text{VH}_2$  A01-B02 blocked authentic SARS-CoV-2 viral entry with  $\text{IC}_{50}$  values of 3.98 nM, 33.5 nM, 12.0 nM and 26.2 nM, respectively (Fig. 4e and Supplementary Table 6).

**Cryo-EM confirms multivalent binding of  $\text{VH}_3$  B01 to Spike.** To confirm whether our linking strategy could successfully engage multiple RBDs on Spike, we obtained a 3.2-Å global resolution cryo-EM three-dimensional (3D) reconstruction of SARS-CoV-2  $S_{\text{ecto}}$  in complex with  $\text{VH}_3$  B01, the most potent neutralizer (Fig. 5a, Extended Data Fig 6, Supplementary Fig. 10 and Supplementary Table 7). Although the S2 region of  $S_{\text{ecto}}$  was resolved at the reported resolution, the RBDs with the bound VH domains were resolved at ~6-Å resolution. However, even at this resolution, the structure unambiguously showed that the three RBDs on Spike are in a two ‘up’ and one ‘down’ conformation. Densities corresponding to each VH domain are present on all three RBDs, indicating that VH B01 can bind both ‘up’ and ‘down’ conformations of RBD. SARS-CoV-2 Spike is rarely observed in this conformation, with most structures being in all RBD ‘down’ state or one RBD ‘up’ state<sup>4,6,32,37</sup>. The binding epitope of VH B01 overlaps with the known ACE2 binding site (Fig. 5b), confirming the intended mechanism of neutralization and validating the ability of the masked selection strategy to precisely direct a binder toward the intended surface on a target protein. To further investigate the dependence of binding on Spike conformation, we performed BLI experiments with  $S_{\text{ecto}}$  at pH 4.5, which has been reported recently to lock Spike in an ‘all-down’ RBD conformation<sup>38</sup>. Binding of both  $\text{VH}_3$  B01 and  $\text{VH}_2$  A01-B01 to  $S_{\text{ecto}}$  were greatly diminished (Extended Data Fig. 7). This observation suggests that one or more RBDs in the ‘up’ conformation may be required for VH B01 to access multiple RBDs on Spike.

## Discussion

Here, we describe a straightforward strategy to rapidly generate linked single-domain binders that potently neutralize SARS-CoV-2. We began by creating and validating a diverse human VH-phage

library and generating VH binders to the ACE2 binding interface of Spike-RBD by a masked selection approach. From a panel of 85 unique VH binders, three were identified that recognized two separate epitopes within the ACE2 binding interface with nanomolar affinity. To engage multiple epitopes simultaneously within an RBD or across RBDs on Spike, these VH monomers were linked into multivalent and bi-paratopic formats by Gly-Ser linkers or Fc domains, without any further high-resolution structural information. This linkage approach not only significantly enhanced affinity, but also substantially improved the viral neutralization potency. We confirmed the basis of this increase by obtaining a cryo-EM structure of the most potent trivalent VH bound to Spike. Consistent with our original design, the trivalent VH simultaneously blocked the ACE2 binding site on all three RBDs of Spike.

We show that the *in vitro* binding affinities and neutralization potencies against this oligomeric target can be dramatically increased with valency. This is exemplified by VH B01, which shows a 460-fold increase in binding affinity and 1,400-fold increase in pseudotyped virus neutralization from VH B01 to  $\text{VH}_2$  B01 to  $\text{VH}_3$  B01. The cryo-EM structure of  $\text{VH}_3$  B01 shows that this binder neutralizes SARS-CoV-2 by blocking the ACE2 binding site on all three RBDs on Spike. Although there could be other contributing neutralization mechanisms such as viral aggregation induced by inter-Spike or inter-virion binding by the multivalent VH, the relatively short linker length (20 amino acids) between the VH domains would make these long-distance interactions significantly less likely. Additionally, no aggregates or  $S_{\text{ecto}}$  multimers induced by  $\text{VH}_3$  B01 were observed during cryo-EM sample preparation and data collection, which further suggests that inter-Spike or inter-virion binding effects, if present, are minimal.

A similar relationship between valency and potency is observed for VH B02, which also targets the same epitope (site B). However, VH A01, which targets site A, is mechanistically distinct, as there is no change in potency between a bivalent ( $\text{VH}_2$ ) and a trivalent ( $\text{VH}_3$ ) format. This suggests that, unlike site B binders, the trivalent site A binder may not be able to fully engage all three RBDs. This could be due to the specific binding mechanism and epitope of VH A01, conformational differences of the RBDs within the Spike trimer or spatial constraints of the linker. Structure determination of site A binders in complex with Spike can elucidate the mechanistic and geometric difference between site A and site B epitopes. Additionally, structure-guided approaches to optimize linker lengths and orientations, coupled with an affinity maturation

campaign, may enable further increases in potency beyond what is demonstrated in this study.

Interestingly, we observed a difference in the cooperativity of the pseudotyped virus neutralization curves between bivalent VH<sub>2</sub> that target both site A and site B (bi-paratopic) versus VH<sub>2</sub> that target only site A or site B (mono-paratopic). Despite similar IC<sub>50</sub> values, the IC<sub>95</sub> values for bi-paratopic VH<sub>2</sub> (VH<sub>2</sub> A01-B01 and VH<sub>2</sub> A01-B02) were much lower than mono-paratopic VH<sub>2</sub> binders. This could indicate a mechanistic difference between these two types of bivalent binder. Bivalent VH<sub>2</sub> can engage multiple RBDs, but only two of the three RBDs can be occluded efficiently, leaving one RBD accessible to ACE2. This could underlie why the neutralization of mono-paratopic VH<sub>2</sub> does not reach 100% compared to, say, a trivalent VH<sub>3</sub>. Curiously, however, the bi-paratopic VH<sub>2</sub> can fully neutralize virus, despite also having only two VH domains. We reason that intra-RBD avidity may play an important and unique role in the neutralization mechanism of bi-paratopic VH<sub>2</sub>. Mono-paratopic binders are limited to inter-RBD avidity and, regardless of valency, are limited to up to three binding sites on Spike. By contrast, bi-paratopic VH<sub>2</sub> can utilize up to six binding epitopes on Spike and utilize both inter-RBD and intra-RBD avidity. Additionally, a more complete occlusion of the ACE2 binding interface (~864 Å<sup>2</sup>)<sup>39</sup> on RBD by the bi-paratopic VH<sub>2</sub> could also underlie this difference in neutralization profiles. Although we do not have a structure of VH<sub>2</sub> A01-B01, we know both A01 and B01 can bind simultaneously within the ACE2 binding site. The cryo-EM structure for B01 shows good coverage of the ACE2 binding site (Fig. 5b) while leaving open adjacent space for VH A01 to occupy a non-overlapping epitope. A better understanding of the binding and neutralization mechanisms of bi-paratopic binders remain a current area of investigation and could lead to the engineering of more potent, multi-specific binders.

Previous studies that utilized designed ankyrin repeat proteins (DARPins), llama-derived nanobodies, computationally designed proteins and bivalent Fabs inspired our engineering strategy<sup>40–46</sup>. We believe our human-derived VH domains offer distinct advantages. Foremost, they would not require the time-consuming structure-guided humanization process that would be necessary for therapeutic nanobody development. Additionally, the VH domains derived from our library have favorable biophysical properties derived from a shared well-behaved scaffold. Our most potent construct, VH<sub>3</sub> B01, retains high-affinity binding after lyophilization cycles. This factor, coupled with scalable production in bacterial systems, may enable lung delivery via inhalation and could facilitate rapid deployment in response to a pandemic. Despite these advantages, single-domain binders have comparatively lower stability and in vivo half-life than mAbs and, due to their novelty, pharmacodynamic properties, such as the prevalence of anti-drug antibodies, have not been as extensively tested in the clinic. Despite these challenges, the engineering potential of these single-domain binders is immense and provides an exciting avenue for the next generation of therapeutic antibody engineering and development. Our results illustrate this potential through a straightforward and rapid strategy to improve the efficacy of single-domain binders and could be applied to other protein interfaces of interest, including future viral proteins and other antigens associated with human disease.

## Online content

Any methods, additional references, Nature Research reporting summaries, source data, extended data, supplementary information, acknowledgements, peer review information; details of author contributions and competing interests; and statements of data and code availability are available at <https://doi.org/10.1038/s41589-020-00679-1>.

Received: 5 August 2020; Accepted: 25 September 2020;  
Published online: 20 October 2020

## References

- Yan, R. et al. Structural basis for the recognition of SARS-CoV-2 by full-length human ACE2. *Science* **367**, 1444–1448 (2020).
- Abraham, J. Passive antibody therapy in COVID-19. *Nat. Rev. Immunol.* **20**, 401–403 (2020).
- Robbiani, D. F. et al. Convergent antibody responses to SARS-CoV-2 in convalescent individuals. *Nature* **584**, 437–442 (2020).
- Pinto, D. et al. Cross-neutralization of SARS-CoV-2 by a human monoclonal SARS-CoV antibody. *Nature* **583**, 290–295 (2020).
- Rogers, T. F. et al. Isolation of potent SARS-CoV-2 neutralizing antibodies and protection from disease in a small animal model. *Science* **7520**, eabc7520 (2020).
- Cao, Y. et al. Potent neutralizing antibodies against SARS-CoV-2 identified by high-throughput single-cell sequencing of convalescent patients' B cells. *Cell* **182**, 73–84 (2020).
- Shi, R. et al. A human neutralizing antibody targets the receptor binding site of SARS-CoV-2. *Nature* **584**, 120–124 (2020).
- Miersch, S. et al. Scalable high throughput selection from phage-displayed synthetic antibody libraries. *J. Vis. Exp.* 1–15 (2015); <https://doi.org/10.3791/51492>
- Nguyen, V. K., Hamers, R., Wyns, L. & Muyldermans, S. Camel heavy-chain antibodies: diverse germline V(H)H and specific mechanisms enlarge the antigen-binding repertoire. *EMBO J.* **19**, 921–930 (2000).
- Holt, L. J., Herring, C., Jespers, L. S., Woolven, B. P. & Tomlinson, I. M. Domain antibodies: proteins for therapy. *Trends Biotechnol.* **21**, 484–490 (2003).
- Ingram, J. R., Schmidt, F. I. & Ploegh, H. L. Exploiting nanobodies' singular traits. *Annu. Rev. Immunol.* **36**, 695–715 (2018).
- Hamer-Casterman, C. & Atarchouch, T. et al. Naturally occurring antibodies devoid of light chains. *Nature* **363**, 446–448 (1998).
- De Genst, E. et al. Molecular basis for the preferential cleft recognition by dromedary heavy-chain antibodies. *Proc. Natl Acad. Sci. USA* **103**, 4586–4591 (2006).
- Arbabi-Ghahroudi, M., Tanha, J. & MacKenzie, R. Prokaryotic expression of antibodies. *Cancer Metastasis Rev.* **24**, 501–519 (2005).
- Zimmermann, I. et al. Synthetic single domain antibodies for the conformational trapping of membrane proteins. *eLife* **7**, 1–32 (2018).
- McMahon, C. et al. Yeast surface display platform for rapid discovery of conformationally selective nanobodies. *Nat. Struct. Mol. Biol.* **25**, 289–296 (2018).
- Saerens, D., Ghassabeh, G. H. & Muyldermans, S. Single-domain antibodies as building blocks for novel therapeutics. *Curr. Opin. Pharmacol.* **8**, 600–608 (2008).
- Nilvebrant, J., Tessier, P. & Sidhu, S. Engineered autonomous human variable domains. *Curr. Pharm. Des.* **22**, 6527–6537 (2016).
- Rouet, R., Dudgeon, K., Christie, M., Langley, D. & Christ, D. Fully human VH single domains that rival the stability and cleft recognition of camelid antibodies. *J. Biol. Chem.* **290**, 11905–11917 (2015).
- Sun, Z. et al. Potent neutralization of SARS-CoV-2 by human antibody heavy-chain variable domains isolated from a large library with a new stable scaffold. *MAbs* **12**, 1778435 (2020).
- Huo, J. et al. Neutralizing nanobodies bind SARS-CoV-2 spike RBD and block interaction with ACE2. *Nat. Struct. Mol. Biol.* **27**, 846–854 (2020).
- Walter, J. D. et al. Sybodies targeting the SARS-CoV-2 receptor-binding domain. Preprint at *bioRxiv* <https://doi.org/10.1101/2020.04.16.045419> (2020).
- Palomo, C. et al. Trivalency of a nanobody specific for the human respiratory syncytial virus fusion glycoprotein drastically enhances virus neutralization and impacts escape mutant selection. *Antimicrob. Agents Chemother.* **60**, 6498–6509 (2016).
- Carter, P. et al. Humanization of an anti-p185HER2 antibody for human cancer therapy. *Proc. Natl Acad. Sci. USA* **89**, 4285–4289 (1992).
- Harmsen, M. M. et al. Llama heavy-chain V regions consist of at least four distinct subfamilies revealing novel sequence features. *Mol. Immunol.* **37**, 579–590 (2000).
- Ma, X., Barthelemy, P. A., Rouge, L., Wiesmann, C. & Sidhu, S. S. Design of synthetic autonomous VH domain libraries and structural analysis of a VH domain bound to vascular endothelial growth factor. *J. Mol. Biol.* **425**, 2247–2259 (2013).
- Dudgeon, K. et al. General strategy for the generation of human antibody variable domains with increased aggregation resistance. *Proc. Natl Acad. Sci. USA* **109**, 10879–10884 (2012).
- Birtalan, S. et al. The intrinsic contributions of tyrosine, serine, glycine and arginine to the affinity and specificity of antibodies. *J. Mol. Biol.* **377**, 1518–1528 (2008).
- Hornsby, M. et al. A high throughput platform for recombinant antibodies to folded proteins. *Mol. Cell. Proteomics* **14**, 2833–2847 (2015).
- Martinko, A. J. et al. Targeting RAS-driven human cancer cells with antibodies to upregulated and essential cell-surface proteins. *eLife* **7**, e31098 (2018).

31. Kabat, E. A., Wu, T. T., Reid-Miller, M., Perry, H. & Gottesman, K. *Sequences of Proteins of Immunological Interest* (US Department of Health and Human Services, Public Health Service, National Institutes of Health, 1987); [https://doi.org/10.1016/0003-2697\(84\)90805-4](https://doi.org/10.1016/0003-2697(84)90805-4)
32. Wrapp, D. et al. Cryo-EM structure of the 2019-nCoV spike in the prefusion conformation. *Science* **367**, 1260–1263 (2020).
33. Lui, I. et al. Trimeric SARS-CoV-2 Spike interacts with dimeric ACE2 with limited intra-Spike avidity. Preprint at *bioRxiv* <https://doi.org/10.1101/2020.05.21.109157> (2020).
34. Neuman, B. W. et al. Supramolecular architecture of severe acute respiratory syndrome coronavirus revealed by electron cryomicroscopy. *J. Virol.* **80**, 7918–7928 (2006).
35. Byrnes, J. R. et al. Competitive SARS-CoV-2 serology reveals most antibodies targeting the Spike receptor-binding domain compete for ACE2 binding. *mSphere* **5**, e00802–e00820 (2020).
36. Crawford, K. H. D. et al. Protocol and reagents for pseudotyping lentiviral particles with SARS-CoV-2 spike protein for neutralization assays. *Viruses* **12**, 513 (2020).
37. Walls, A. C. et al. Structure, function and antigenicity of the SARS-CoV-2 spike glycoprotein. *Cell* **180**, 281–292 (2020).
38. Zhou, T. et al. A pH-dependent switch mediates conformational masking of SARS-CoV-2 spike. Preprint at *bioRxiv* <https://doi.org/10.1101/2020.07.04.187989> (2020).
39. Lan, J. et al. Structure of the SARS-CoV-2 spike receptor-binding domain bound to the ACE2 receptor. *Nature* **581**, 215–220 (2020).
40. Dong, J. et al. Development of multi-specific humanized llama antibodies blocking SARS-CoV-2/ACE2 interaction with high affinity and avidity. *Emerg. Microbes Infect.* **9**, 1034–1036 (2020).
41. Binz, H. K., Amstutz, P. & Plückthun, A. Engineering novel binding proteins from nonimmunoglobulin domains. *Nat. Biotechnol.* **23**, 1257–1268 (2005).
42. Binz, H. K., Stumpf, M. T., Forrer, P., Amstutz, P. & Plückthun, A. Designing repeat proteins: well-expressed, soluble and stable proteins from combinatorial libraries of consensus ankyrin repeat proteins. *J. Mol. Biol.* **332**, 489–503 (2003).
43. Binz, H. K. et al. Design and characterization of MP0250, a tri-specific anti-HGF/anti-VEGF DARPin® drug candidate. *MAbs* **9**, 1262–1269 (2017).
44. Conrath, K. E., Lauwereys, M., Wyns, L. & Muyllydermans, S. Camel single-domain antibodies as modular building units in bispecific and bivalent antibody constructs. *J. Biol. Chem.* **276**, 7346–7350 (2001).
45. Strauch, E. M. et al. Computational design of trimeric influenza-neutralizing proteins targeting the hemagglutinin receptor binding site. *Nat. Biotechnol.* **35**, 667–671 (2017).
46. Galimidi, R. P. et al. Intra-Spike crosslinking overcomes antibody evasion by HIV-1. *Cell* **160**, 433–446 (2015).

**Publisher's note** Springer Nature remains neutral with regard to jurisdictional claims in published maps and institutional affiliations.

© The Author(s), under exclusive licence to Springer Nature America, Inc. 2020

## CryoEM grid freezing/collection team

**Caleigh M. Azumaya<sup>7</sup>, Julian R. Braxton<sup>7</sup>, Axel F. Brilot<sup>7</sup>, Meghna Gupta<sup>7</sup>, Fei Li<sup>7</sup>, Kyle E. Lopez<sup>7</sup>, Arthur Melo<sup>7</sup>, Gregory E. Merz<sup>7</sup>, Frank Moss<sup>7</sup>, Joana Paulino<sup>7</sup>, Thomas H. Pospiech Jr.<sup>7</sup>, Sergei Pourmal<sup>7</sup>, Cristina Puchades<sup>7</sup>, Alexandria N. Rizo<sup>7</sup>, Amber M. Smith<sup>7</sup>, Ming Sun<sup>7</sup>, Paul V. Thomas<sup>7</sup>, Feng Wang<sup>7</sup> and Zanlin Yu<sup>7</sup>**

## CryoEM data processing team

**Daniel Asarnow<sup>7</sup>, Julian R. Braxton<sup>7</sup>, Melody G. Campbell<sup>7</sup>, Cynthia M. Chio<sup>7</sup>, Un Seng Chio<sup>7</sup>, Miles Sasha Dickinson<sup>7</sup>, Devan Diwanji<sup>7</sup>, Bryan Faust<sup>7</sup>, Meghna Gupta<sup>7</sup>, Nick Hoppe<sup>7</sup>, Mingliang Jin<sup>7</sup>, Fei Li<sup>7</sup>, Junrui Li<sup>7</sup>, Yanxin Liu<sup>7</sup>, Gregory E. Merz<sup>7</sup>, Henry C. Nguyen<sup>7</sup>, Joana Paulino<sup>7</sup>, Thomas H. Pospiech Jr.<sup>7</sup>, Sergei Pourmal<sup>7</sup>, Smriti Sangwan<sup>7</sup>, Raphael Trenker<sup>7</sup>, Donovan Trinidad<sup>7</sup>, Eric Tse<sup>7</sup>, Kaihua Zhang<sup>7</sup> and Fengbo Zhou<sup>7</sup>**

## Mammalian cell expression team

**Caleigh M. Azumaya<sup>7</sup>, Christian Billesboelle<sup>7</sup>, Alisa Bowen<sup>7</sup>, Melody G. Campbell<sup>7</sup>, Devan Diwanji<sup>7</sup>, Nick Hoppe<sup>7</sup>, Yen-Li Li<sup>7</sup>, Phuong Nguyen<sup>7</sup>, Carlos Nowotny<sup>7</sup>, Cristina Puchades<sup>7</sup>, Mali Safari<sup>7</sup>, Smriti Sangwan<sup>7</sup>, Kaitlin Schaefer<sup>7</sup>, Amber M. Smith<sup>7</sup>, Raphael Trenker<sup>7</sup>, Tsz Kin Martin Tsui<sup>7</sup>, Natalie Whitis<sup>7</sup> and Jianhua Zhao<sup>7</sup>**

## Protein purification team

**Daniel Asarnow<sup>7</sup>, Caleigh M. Azumaya<sup>7</sup>, Cynthia M. Chio<sup>7</sup>, Bryan Faust<sup>7</sup>, Meghna Gupta<sup>7</sup>, Kate Kim<sup>7</sup>, Michelle Moritz<sup>7</sup>, Tristan W. Owens<sup>7</sup>, Joana Paulino<sup>7</sup>, Jessica K. Peters<sup>7</sup>, Sergei Pourmal<sup>7</sup>, Kaitlin Schaefer<sup>7</sup> and Tsz Kin Martin Tsui<sup>7</sup>**

**Crystallography team**

**Justin Biel<sup>7</sup>, Ishan Deshpande<sup>7</sup>, Nadia Herrera<sup>7</sup>, Huong T. Kratochvil<sup>7</sup>, Xi Liu<sup>7</sup>, Ursula Schulze-Gahmen<sup>7</sup> and Iris D. Young<sup>7</sup>**

**Bacterial expression team**

**Jen Chen<sup>7</sup>, Amy Diallo<sup>7</sup>, Loan Doan<sup>7</sup>, Sebastian Flores<sup>7</sup>, Meghna Gupta<sup>7</sup>, Mingliang Jin<sup>7</sup>,  
Huong T. Kratochvil<sup>7</sup>, Victor L. Lam<sup>7</sup>, Yang Li<sup>7</sup>, Megan Lo<sup>7</sup>, Gregory E. Merz<sup>7</sup>, Joana Paulino<sup>7</sup>,  
Aye C. Thwin<sup>7</sup>, Erron W. Titus<sup>7</sup>, Zanlin Yu<sup>7</sup>, Fengbo Zhou<sup>7</sup> and Yang Zhang<sup>7</sup>**

**Infrastructure team**

**David Bulkley<sup>7</sup>, Arceli Joves<sup>7</sup>, Almarie Joves<sup>7</sup>, Liam McKay<sup>7</sup>, Mariano Tabios<sup>7</sup> and Eric Tse<sup>7</sup>**

**Leadership team**

**David A. Agard<sup>7</sup>, Yifan Cheng<sup>7</sup>, James S. Fraser<sup>7</sup>, Adam Frost<sup>7</sup>, Natalia Jura<sup>7</sup>, Tanja Kortemme<sup>7</sup>,  
Nevan J. Krogan<sup>7</sup>, Aashish Manglik<sup>7</sup>, Oren S. Rosenberg<sup>7</sup>, Daniel R. Southworth<sup>7</sup>, Robert M. Stroud<sup>7</sup>  
and Kliment A. Verba<sup>7</sup>**

---

<sup>7</sup>Quantitative Biosciences Institute (QBI) Coronavirus Research Group Structural Biology Consortium, University of California San Francisco, San Francisco, CA, USA.

## Methods

**VH library construction and validation by next-generation sequencing.** The VH-phage library was created through bivalent display of VH on the surface of M13 bacteriophage, as previously described<sup>19,47,48</sup>. In brief, the DNA phagemid library was created through oligonucleotide mutagenesis. First, the human VH-4D5 sequence was modified with five mutations (35G/39R/45E/47L/50R) in the framework and with restriction sites in each of the CDRs: AgeI in CDR H1, NcoI in CDR H2 and XhoI in CDR H3 (Supplementary Table 1). Oligonucleotides were synthesized by a custom Trimer Phosphoramidite mix for CDR H1 and CDR H2 (Twist Bioscience) and CDR H3 (Trilink Biotechnologies) (Supplementary Table 2). After mutagenesis, DNA sub-library pools were digested with appropriate restriction enzymes to remove the phagemid template before transformation into SS320 electrocompetent cells (Lucigen) for phage production. NGS of the CDR H3 was performed on the pooled library by amplifying the phagemid from boiled phage with in-house primers. Samples were submitted for analysis on a HiSeq4000 (Illumina) system with a custom primer: TGAGGACACTGCCGTCTATTATTGTGCTCGC ( $T_m = 67^\circ\text{C}$ , GC content = 52%). NGS analysis of the output was performed using an in-house informatics pipeline written in R. In brief, the raw NGS data sequencing file (\*.fastq.gz) was converted into a table composed of the DNA sequences, the amino-acid sequences (CDR H3) and the counts/frequency as columns, then saved as a \*.csv file for further analysis (for example, calculation of amino acid abundance, sequence logo, H3 length distribution and so on). Several filters were applied: (1) low-quality sequences containing 'N' were removed; (2) sequences with any stop codon were removed; (3) only the sequences that were in-frame were kept. Scripts are available for download at [https://github.com/crystaljie/VH\\_library\\_CDR\\_H3\\_NGS\\_analysis\\_Cole.Bracken.git](https://github.com/crystaljie/VH_library_CDR_H3_NGS_analysis_Cole.Bracken.git).

**Cloning, protein expression and purification.** Spike-RBD monomer, Spike-RBD-Fc, Spike ectodomain ( $S_{\text{ecto}}$ ) and ACE2-Fc were produced as biotinylated proteins as previously described<sup>33</sup>. VH were subcloned from the VH-phagemid into *E. coli* expression vector pBL347. VH<sub>1</sub> and VH<sub>3</sub> were cloned into pBL347 with a 20-amino-acid Gly-Ser linker. VH-Fc were cloned into a pFUSE (InvivoGen) vector with a human IgG1 Fc domain. All constructs were sequence-verified by Sanger sequencing. VH, VH<sub>2</sub> and VH<sub>3</sub> constructs were expressed in *E. coli* C43(DE3) Pro+ using optimized autoinduction medium and purified by protein A affinity chromatography, similarly to Fabs (Supplementary Fig. 11)<sup>29</sup>. VH-Fc were expressed in Expi293 BirA cells using transient transfection (ExpiFectamine, Thermo Fisher Scientific). Four days after transfection, the medium was collected and VH-Fc were purified using protein A affinity chromatography. All proteins were buffer-exchanged into PBS by spin concentration and stored in aliquots at  $-80^\circ\text{C}$ . The purity and integrity of proteins were assessed by SDS-PAGE. All proteins were endotoxin-removed using an endotoxin removal kit (Thermo Fisher) before use in neutralization assays.

**Phage selection with the VH-phage library.** Phage selections were performed according to previously established protocols<sup>29</sup>, using biotinylated antigens captured with streptavidin-coated magnetic beads (Promega). In each round, the phage pool was first cleared by incubation with beads loaded with 500 nM ACE2-Fc/Spike-RBD-Fc complex. The unbound phage were then incubated with beads loaded with Spike-RBD-Fc. After washing, the bound phage was eluted by the addition of 2  $\mu\text{g ml}^{-1}$  of tobacco etch virus protease. In total, four rounds of selection were performed with decreasing amounts of Spike-RBD-Fc, as shown in Fig. 2a. All steps were carried out in PBS buffer + 0.02% Tween-20 + 0.2% BSA (PBSTB). Individual phage clones from the third and fourth rounds of selections were analyzed by phage ELISA.

**Phage enzyme-linked immunosorbent assay.** For each phage clone, four different conditions were tested—direct: Spike-RBD-Fc; competition: Spike-RBD-Fc with an equal concentration of Spike-RBD-Fc in solution; negative selection: ACE2-Fc/Spike-RBD-Fc complex; control: Fc. Flat-bottomed clear plates (Nunc MaxiSorp 384-well, Thermo Fisher Scientific) were coated with 0.5  $\mu\text{g ml}^{-1}$  of NeutrAvidin in PBS overnight at  $4^\circ\text{C}$  and subsequently blocked with PBS + 0.02% Tween-20 + 2% BSA for 1 h at room temperature. Plates were washed three times with PBS containing 0.05% Tween-20 (PBST) and were washed similarly between each of the steps, then 20 nM biotinylated Spike-RBD-Fc, ACE2-Fc/Spike-RBD-Fc complex or Fc diluted in PBSTB was captured on the NeutrAvidin-coated wells for 30 min, then blocked with PBSTB + 10  $\mu\text{M}$  biotin for 30 min. Phage supernatant diluted 1:5 in PBSTB was added for 20 min. For the competition samples, the phage supernatant was diluted into PBSTB with 20 nM Spike-RBD-Fc. Bound phage were detected by incubation with anti-M13 antibody conjugated to horseradish-peroxidase (HRP) (Sino Biological; 1:5,000) for 30 min, followed by the addition of 3', 5', 5' tetramethyl benzidine (TMB) substrate (VWR International). The reaction was quenched with the addition of 1 M phosphoric acid, then absorbance at 450 nm was measured using a Tecan M200 Pro spectrophotometer.

**Enzyme-linked immunosorbent assay half-maximum effective concentration with Spike-RBD-monomer.** Flat-bottomed clear plates (384-well Nunc Maxisorp)

were prepared similarly to the phage ELISA protocol (above) by coating with neutravidin, followed by blocking with PBST + 2% BSA, incubation with 20 nM Spike-RBD-monomer and blocking by PBSTB + 10  $\mu\text{M}$  biotin. VH binders in fourfold dilutions ranging from 500 nM to 2.8 pM were added for 1 h. Bound VH was detected by incubation with Protein A HRP conjugate (Thermo Fisher Scientific; 1:10,000) for 30 min, followed by the addition of TMB substrate for 5 min, quenching by 1 M phosphoric acid and detection of absorbance at 450 nm. Each concentration was tested in duplicate and the assay repeated three times.

**Bio-layer interferometry experiments.** BLI data were measured using an Octet RED384 (ForteBio) instrument. Spike-RBD or  $S_{\text{ecto}}$  was immobilized on a streptavidin or Ni-NTA biosensor and loaded until a 0.4-nm signal was achieved. After blocking with 10  $\mu\text{M}$  biotin, purified binders in solution were used as the analyte. PBSTB was used for all buffers for BLI at pH 7.4. For BLI at pH 4.5, 10 mM sodium acetate pH 4.5, 150 mM NaCl, 0.2 mg ml<sup>-1</sup> BSA and 0.01% (wt/vol) Tween-20 were used. Data were analyzed using ForteBio Octet analysis software and kinetic parameters were determined using a 1:1 monovalent binding model.

### Competition enzyme-linked immunosorbent assay with COVID-19 convalescent patient sera.

Competition ELISA with convalescent patient sera was conducted with the same patient sera as previously reported<sup>35</sup>. Samples were collected in accordance with the Declaration of Helsinki using protocols approved by the UCSF Institutional Review Board (protocol 20-30338). Patients were voluntarily recruited based on their history of previous SARS-CoV-2 infection. All patients provided written consent. Patient sera were de-identified before delivery to the Wells Lab, where all experiments presented here were performed. Briefly, sera were obtained, as described, from patients with a history of a positive test with nasopharyngeal SARS-CoV-2 PCR with reverse transcription PCR (RT-PCR) and at least 14 days after the resolution of their COVID-19 symptoms. Healthy control serum was obtained before the emergence of SARS-CoV-2. Sera were heat-inactivated ( $56^\circ\text{C}$  for 60 min) before use. Competitive serology using biotinylated SARS-CoV-2 Spike-RBD as the capture antigen was performed as previously reported<sup>35</sup>, but with slight modifications. Instead of supplementing sera diluted 1:50 in 1% nonfat milk with 100 nM ACE2-Fc, each of the indicated VH-Fc fusions was used at 100 nM. Bound patient antibodies were then detected using Protein L-HRP (Thermo Fisher Scientific 32420, 1:5,000). Background from the raw ELISA signal in serum-treated wells was removed by first subtracting the signal measured in NeutrAvidin-alone coated wells, then subtracting the signal detected in antigen-coated wells incubated with 1% nonfat milk + 100 nM competitor.

### Differential scanning fluorimetry.

DSF was conducted as previously described<sup>29</sup>. Briefly, purified protein was diluted to 0.5  $\mu\text{M}$  or 0.25  $\mu\text{M}$  in buffer containing Sypro Orange 4x (Invitrogen) and PBS and assayed in a 384-well white PCR plate. All samples were tested in duplicate. In a Roche LC480 LightCycler, the sample was heated from  $30^\circ\text{C}$  to  $95^\circ\text{C}$  with a ramp rate of  $0.3^\circ\text{C}$  per 30 s, and the fluorescence signals at 490 nm and 575 nm were continuously collected.  $T_m$  was calculated using the Roche LC480 LightCycler software.

**Size exclusion chromatography.** SEC analysis was performed using an Äkta Pure system (GE Healthcare) using a Superdex 200 Increase 10/300 GL column. A 100  $\mu\text{l}$  volume of 2–3 mg ml<sup>-1</sup> of each analyte was injected and run with a constant mobile phase of degassed 10 mM Tris pH 8.0 and 200 mM NaCl. The absorbance at 280 nm was measured. Post-lyophilization and reconstitution SEC was performed using an Agilent HPLC 1260 Infinity II LC system using an AdvanceBio SEC column (300  $\text{\AA}$ , 2.7  $\mu\text{m}$ , Agilent). Fluorescence (excitation 285 nm, emission 340 nm) was measured.

### Preparation of SARS-CoV-2 pseudotyped virus and the HEK-ACE2 overexpression cell line.

HEK293T-ACE2 cells were a gift from A. Wiita's laboratory at the University of California, San Francisco. Cells were cultured in D10 medium (DMEM + 1% pen-strep + 10% heat-inactivated FBS). Plasmids to generate pseudotyped virus were a gift from P. Kim's lab at Stanford University and SARS-CoV-2 pseudotyped virus was prepared as previously described<sup>36</sup>. Briefly, plasmids at the designated concentrations were added to OptiMEM medium with FuGENE HD transfection reagent (Promega) at a 3:1 FuGENE:DNA ratio, incubated for 30 min, and subsequently transfected into HEK293T cells. After 24 h, the supernatant was removed and replaced with D10 culture medium. Virus was propagated for an additional 48 h, and the supernatant was collected and filtered. Virus was stored at  $4^\circ\text{C}$  for up to 10 days.

HEK-ACE2 were seeded at 10,000 cells per well on 96-well white plates (Corning, cat. no. 354620). After 24 h, pseudotyped virus stocks were titrated via a twofold dilution series in D10 medium, and 40  $\mu\text{l}$  was added to cells. After 60 h, infection and the intracellular luciferase signal were determined using a Bright-Glo luciferase assay (Promega), and the dilution achieving maximal luminescent signal within the linear range,  $\sim 3\text{--}5 \times 10^5$  luminescence units, was chosen as the working concentration for neutralization assays. Pseudovirus stocks were flash-frozen in aliquots and stored at  $-80^\circ\text{C}$  and thawed on ice just before use in a neutralization assay.

**Pseudotyped viral neutralization assays.** HEK-ACE2 cells were seeded at 10,000 cells per well in 40 µl of D10 on 96-well white plates (Corning, cat. no. 354620) 24 h before infection. To determine the IC<sub>50</sub> values for pseudotyped virus, dose series of each VH binder were prepared at 3× concentration in D10 medium and 50 µl samples were aliquoted into each well in a 96-well plate format. Next, 50 µl of virus diluted in D10 medium was added to each well and the virus and blocker solution were allowed to incubate for 1 h at 37 °C. Subsequently, 80 µl of the virus and blocker solution were transferred to wells seeded with HEK-ACE2. After 60 h of infection at 37 °C, the intracellular luciferase signal was measured using a Bright-Glo luciferase assay: 80 µl of reconstituted Bright-Glo luciferase reagent was added to each well, incubated at room temperature with gentle shaking for 5 min, before the luminescence was measured on a Tecan M200 Pro spectrophotometer. The IC<sub>50</sub> was determined using a four-parameter nonlinear regression (GraphPad Prism).

**Authentic viral neutralization assays.** Authentic virus neutralization assays were carried out as previously described<sup>33</sup>. All handling and experiments using live SARS-CoV-2 virus clinical isolate 2019-nCoV/USA-WA1/2020 (BEI Resources) was conducted under BSL3 containment with approved Biohazard Use Authorization (BUA) and protocols. VeroE6 cells were cultured in minimal essential medium (MEM), 10% FBS and 1% pen-strep. For neutralization assays, VeroE6 cells were seeded on six-well culture plates at 3.8 × 10<sup>5</sup> cells per well the day before. Infection with SARS-CoV-2 was performed using a multiplicity of infection (MOI) of 0.1. Virus was incubated in infection medium (EMEM 0% FBS) containing different concentrations of binders for 1 h at 37 °C. Culture medium was removed from the VeroE6 cells and 300 µl of the blocker/virus inoculum was added to the cells for 1 h at 37 °C. After this step, 1 ml of EMEM with 10% FBS was added to the cells, and the cells were incubated at 37 °C for an additional 16 h before RNA collection. Viral entry into cells and cellular transcription of viral genes was measured by qPCR using the N gene and host beta-glucuronidase (GUSB) and host beta-actin (ACTB) as controls. An RNAeasy RNA extraction kit (Qiagen) was used for RNA extraction and a Quantitect reverse-transcriptase kit (Qiagen) was used to generate cDNA. qPCR reactions were prepared using SYBR Select Master Mix (Thermo). The N gene and hGUSB gene primer concentration was 400 nM and the annealing temperature was 58 °C. Primer sequences (IDT) were as follows—viral N gene: N\_F=CACATTGGCACCCGAATC; N\_R=GAGGAACGAGAAAGAGGCTTG; host gene: hGUSB\_F=CTCATCTGGAATTTCGCCATT; hGUSB\_R=CCGAGTGAAGACCCCCTTTTA. The relative copy number (RCN) of viral transcript level compared to the host transcript was determined using the ΔΔCT method. IC<sub>50</sub> values were determined using a four-parameter nonlinear regression (GraphPad Prism).

**Expression and purification of the Spike ectodomain for cryo-electron microscopy.** To obtain the pre-fusion Spike ectodomain, methods similar to those in previous reports were used<sup>32,49</sup>. The expression plasmid, provided by the McLellan lab, was used in a transient transfection with 100 ml, high-density Chinese hamster ovary (ExpiCHO, Thermo Fisher) culture following the ‘High Titer’ protocol provided by Thermo Fisher. Six to nine days post transfection, the supernatant was collected with centrifugation at 4,000g at room temperature. The clarified supernatant was then incubated with Ni-Sepharose Excel resin (Cytiva Life Sciences) for 90 min at room temperature. After incubation, the nickel resin was washed with 20 mM Tris (pH 8), 200 mM NaCl and 20 mM imidazole with 10 column volumes. Protein was eluted from the nickel resin with 20 mM Tris (pH 8), 200 mM NaCl and 500 mM imidazole. Eluate was then concentrated with a 50 molecular weight cutoff Amicon Ultra-15 centrifugal unit by centrifugation at 2,500g at room temperature. The eluate was concentrated, filtered with a 0.2-µm filter and injected onto a Superose 6 10/300 GL column equilibrated with 10 mM Tris (pH 8) and 200 mM NaCl. Fractions corresponding to monodisperse Spike were collected and the concentration was determined using a NanoDrop system.

**Cryo-electron microscopy sample preparation, data collection and processing.** Spike ectodomain (2 µM) was mixed with fivefold excess VH<sub>3</sub>B01 and applied (3 µl) to holey-carbon Au 200 mesh 1.2/1.3 Quantifoil grids. Grids were blotted and plunge-frozen using a Mark 4 Vitrobot (Thermo Fisher) at 4 °C and 100% humidity, utilizing blot force 0 and a blot time of 4 s. A total of 1,656 images were collected on a Titan Krios cryo-electron microscope (Thermo Fisher) equipped with a K3 direct detector operated in correlated double sampling (CDS) mode (Gatan Ametek) and an energy filter (Gatan Ametek) at a nominal magnification of ×105,000 (0.834 Å per physical pixel). Dose-fractionated videos were collected with a total exposure of 6 s and 0.04 s per frame at a dose rate of nine electrons per physical pixel per second. Videos were corrected for motion and filtered to account for electron damage utilizing MotionCor2<sup>50</sup>. Drift-corrected sums were imported into the cryoSPARC2 processing package<sup>51</sup>. Micrographs were manually curated, contrast transfer function (CTF) was estimated utilizing patches, and particles were picked with a Gaussian blob. The previous Spike ectodomain structure was imported as an initial model (low-pass-filtered to 30 Å) and multiple rounds of 3D and 2D classification were performed. Images were re-picked with the best looking 2D class averages low-pass-filtered to 30 Å, and multiple rounds of 3D classification

were performed again to obtain a homogeneous stack of Spike trimer particles. The majority of the particles went into classes putatively representing excess unbound VH<sub>3</sub>B01 and the final Spike-like particle stack only contained ~21,000 particles. Non-uniform homogeneous refinement of the particle stack resulted in a global resolution of 3.2 Å (masked) utilizing 0.143 Fourier Shell Correlation (FSC) cutoff<sup>52</sup>. PDB 6X2B was rigid body fit into the resulting reconstruction in UCSF Chimera<sup>53</sup>. The RBDs of two Spike trimers were moved as a rigid body to accommodate the cryo-EM density. The cryo-EM reconstruction was low-pass-filtered to 6 Å to better visualize the VH densities. The homology model was built based on PDB 4G80 for the VH domains, and the resulting and individual VH domains were rigid body fit into the 6-Å cryo-EM density as depicted in Fig. 5a. The resulting model was relaxed into the cryo-EM map low-pass-filtered to 6 Å with the Rosetta FastRelax protocol. For Supplementary Fig. 13 the local resolution was estimated using ResMap<sup>54</sup>. The final figures were prepared using ChimeraX<sup>55</sup>.

**Reporting Summary.** Further information on research design is available in the Nature Research Reporting Summary linked to this Article.

## Data availability

Cryo-EM structural data have been deposited in the Protein Data Bank and Electron Microscopy Data Bank, (PDB 7JWB and EMD-22514). The cryo-EM structure of the Spike trimer from PDB 6VSB and ACE2 from PDB 6M17 and PDB 6M0J were used for distance estimates. The cryo-EM structure of Spike trimer from PDB 6X2B and the crystal structure of a VH domain from PDB 3P9W were used for cryo-EM data processing. Source data are provided with this paper. Any additional information is available upon request.

## Code availability

Code used to analyze the NGS data has been deposited in GitHub and is available for download at [https://github.com/crystaljie/VH\\_library\\_CDR\\_H3\\_NGS\\_analysis\\_Cole.Bracken.git](https://github.com/crystaljie/VH_library_CDR_H3_NGS_analysis_Cole.Bracken.git).

## References

47. Lee, C. V. et al. High-affinity human antibodies from phage-displayed synthetic Fab libraries with a single framework scaffold. *J. Mol. Biol.* **340**, 1073–1093 (2004).
48. Chen, G. & Sidhu, S. S. Design and generation of synthetic antibody libraries for phage display. *Methods Mol. Biol.* **1131**, 113–131 (2014).
49. Wang, B. et al. Bivalent binding of a fully human IgG to the SARS-CoV-2 spike proteins reveals mechanisms of potent neutralization. Preprint at *bioRxiv* <https://doi.org/10.1101/2020.07.14.203414> (2020).
50. Zheng, S. Q. et al. MotionCor2: anisotropic correction of beam-induced motion for improved cryo-electron microscopy. *Nat. Methods* **14**, 331–332 (2017).
51. Punjani, A., Rubinstein, J. L., Fleet, D. J. & Brubaker, M. A. CryoSPARC: algorithms for rapid unsupervised cryo-EM structure determination. *Nat. Methods* **14**, 290–296 (2017).
52. Punjani, A., Zhang, H. & Fleet, D. J. Non-uniform refinement: adaptive regularization improves single particle cryo-EM reconstruction. Preprint at *bioRxiv* <https://doi.org/10.1101/2019.12.15.877092> (2019).
53. Pettersen, E. F. et al. UCSF Chimera—a visualization system for exploratory research and analysis. *J. Comput. Chem.* **25**, 1605–1612 (2004).
54. Kucukelbir, A., Sigworth, F. J. & Tagare, H. D. Quantifying the local resolution of cryo-EM density maps. *Nat. Methods* **11**, 63–65 (2014).
55. Goddard, T. D. et al. UCSF ChimeraX: meeting modern challenges in visualization and analysis. *Protein Sci.* **27**, 14–25 (2018).

## Acknowledgements

We thank members of the Wells Lab, particularly those working on COVID-19 projects, for their efforts and contributions. Specifically, we would like to thank J. Gramespacher for purifying binders and M. Nix (UCSF) for guidance on pseudotyped virus neutralization assays. Additionally, we thank the entire QCRC for its rapid large-scale collaborative effort. Specifically, we thank C. Puchades and C. Azumaya for their efforts in the optimization of cryo-EM grid freezing and data collection, T. Owens for assistance in protein purification, D. Diwanji for expression of S<sub>ecto</sub> and A. Manglik (UCSF) for advice on cryo-EM experiments and protein purification. We also thank the laboratory of P. Kim (Stanford University) for providing plasmids for pseudotyped virus production. Finally, we thank M. Wilson, C. Chiu and R. Loudermilk (UCSF), as well as the patients, for providing convalescent sera. J.A.W. is supported by generous grants from NCI (R35 GM122451-01); the Chan-Zuckerberg Biohub, UCSF Program for Breakthrough Biomedical Research (PBBR); Fast Grants from Emergent Ventures at the Mercatus Center, George Mason University (#2154); and funding from The Harrington Discovery Institute (GA33116). S.A.L. is a Merck Fellow of the Helen Hay Whitney Foundation. K.S. is a Fellow of the Damon Runyon Cancer Research Foundation, DRG-2297-17. J.R.B. and J.Z. are supported by the National Institutes of Health National Cancer Institute (F32 5F32CA239417 (J.R.B.) and 5F32CA236151-02 (J.Z.)). B.S.Z. is supported by the

National Institutes of Health National Cancer Institute (T32, HL007185). N.J.R. and I.L. are supported by the National Science Foundation (GRFP). D.P.N. was the Connie and Bob Lurie Fellow of the Damon Runyon Cancer Research Foundation (DRG-2204-14) and supported by a UCSF-PBMR Postdoctoral Independent Research Award, which is partially funded by the Sandler Foundation.

**QCRG Structural Biology Consortium.** In addition to those listed explicitly in the Author contributions, the structural biology portion of this work was performed by the QCRG (Quantitative Biosciences Institute Coronavirus Research Group) Structural Biology Consortium. Listed below are the contributing members of the consortium listed by teams in order of team relevance to the published work. The team leads (responsible for organization of each team and for the experimental design utilized within each team) are as follows: Cryo-EM grid freezing/collection team—Caleigh M. Azumaya, Cristina Puchades, Ming Sun; Cryo-EM data processing team—Miles Sasha Dickinson, Henry C. Nguyen; Mammalian cell expression team—Christian Billesboelle, Melody G. Campbell, Devan Diwanji, Carlos Nowotny, Amber M. Smith, Jianhua Zhao; Protein purification team—Daniel Asarnow, Michelle Moritz, Tristan W. Owens, Sergei Pournal; Crystallography team—Nadia Herrera, Huong T. Kratochvil, Ursula Schulze-Gahmen, Iris D. Young; Bacterial expression team—Amy Diallo, Meghna Gupta, Erron W. Titus; Leadership team—Oren S. Rosenberg, Kliment A Verba. The QCRG Structural Biology Consortium has received support from the Quantitative Biosciences Institute, the Defense Advanced Research Projects Agency HR0011-19-2-0020 (to D.A.A. and K.A.V.; B. Shiochet PI), a FastGrants COVID19 grant (K.A. Verba PI), the Laboratory for Genomics Research (O.S. Rosenberg PI) and the Laboratory For Genomics Research (R.M. Stroud PI).

## Author contributions

C.J.B. and D.P.N. designed and constructed the VH-phage library. C.J.B., S.A.L., N.J.R., J.Z., I.L., J.L. and K.P. cloned, expressed and purified the VH binders and/or antigens. C.J.B., S.A.L. and J.L. designed and/or conducted the *in vitro* characterization of the VH binders. J.R.B. designed and conducted the competition ELISA assay with convalescent patient sera. P.S., N.J.R. and S.A.L. designed and conducted the pseudovirus neutralization assays. P.S., N.J.R., B.S.Z. and S.A.L. designed and conducted the live virus neutralization assays. K.S. prepared samples for cryo-EM and the QCRG SBC performed cryo-EM data collection and analyses. S.A.L., X.X.Z., K.K.L. and J.A.W. led the coordination of external collaborations and supervised the project. C.J.B., S.A.L. and J.A.W. co-wrote the manuscript with input from all the authors.

## Competing interests

The authors declare no competing interests.

## Additional information

**Extended data** is available for this paper at <https://doi.org/10.1038/s41589-020-00679-1>.

**Supplementary information** is available for this paper at <https://doi.org/10.1038/s41589-020-00679-1>.

**Correspondence and requests for materials** should be addressed to J.A.W.

**Reprints and permissions information** is available at [www.nature.com/reprints](http://www.nature.com/reprints).

CDR H1												
	28	29	30	31	32	33	33a	33b	34	35	36	
Template:	N	I	K	D	T	Y	-	-	I	G	W	
Library:	RAD	IF	YS	YS	YSED	YSED	-	-	I	G	W	
	RAD	IF	YS	YS	YSED	YSED	-	-	I	G	W	
	RAD	IF	YS	YS	YS	YSED	YSED	YSED	I	G	W	

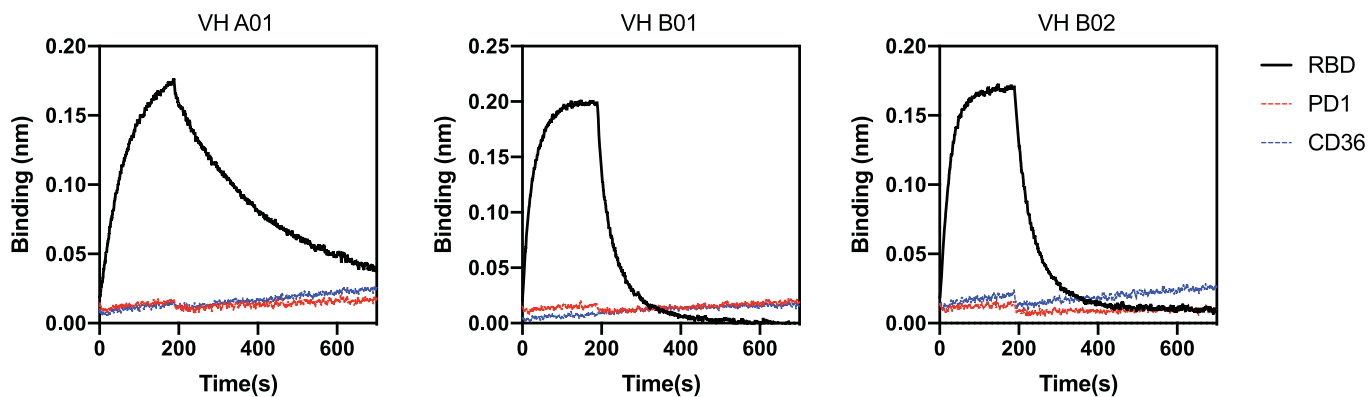
CDR H2												
	49	50	51	52	52a	53	54	55	56	57	58	59
Template:	A	R	I	Y	P	T	N	G	Y	T	R	Y
Library:	A	R	I	YS	PS	YS	YS	SG	YS	T	YS	Y

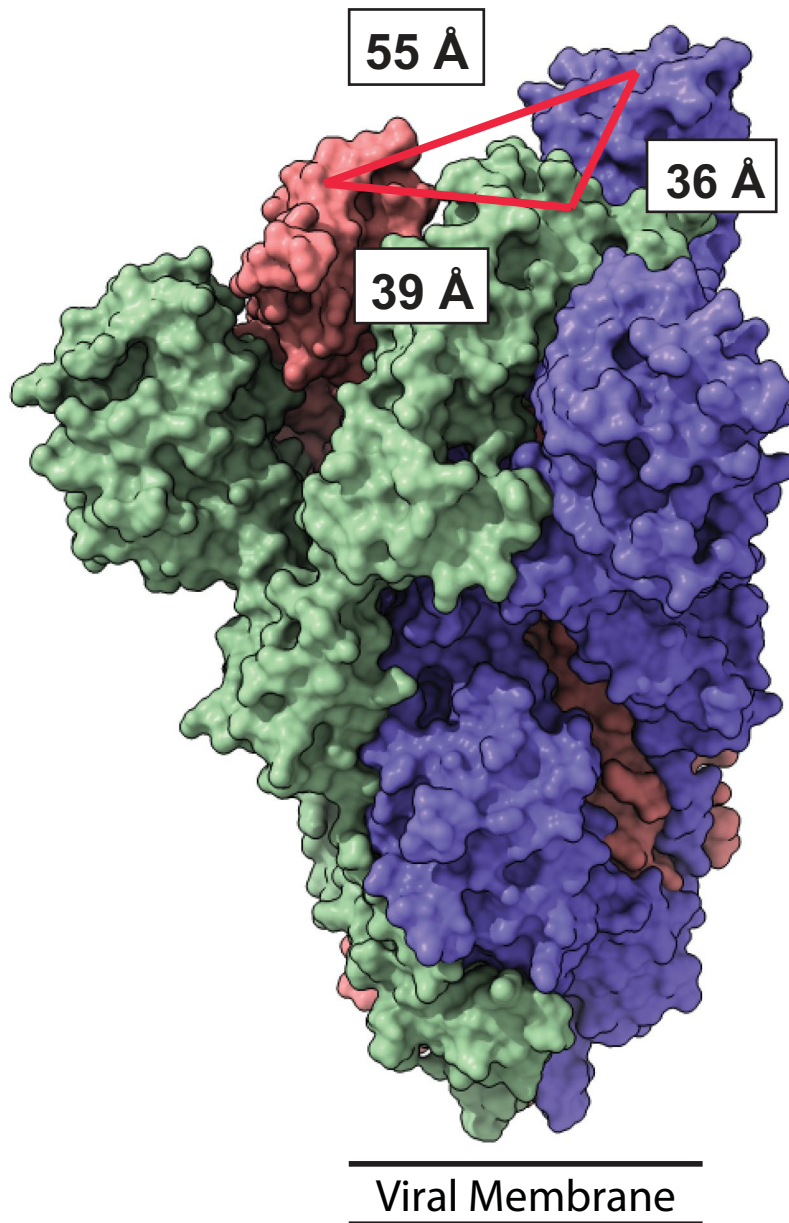
CDR H3												
	94	95	96	97	98	99	100	100a	100b	100c	101	102
Template:	R	W	G	G	D	G	F	Y	A	M	D	Y
Library:	R	X <sub>(2-16)</sub>	-	-	-	-	-	-	AG	FLIM	D	Y

X = Y = 20%, S = 17.5%, G = 15%, D = 10%, A = 7.5%, F = 7.5%,  
W = 7.5%, P = 5%, V = 5%, H = 2.5%, R = 2.5%

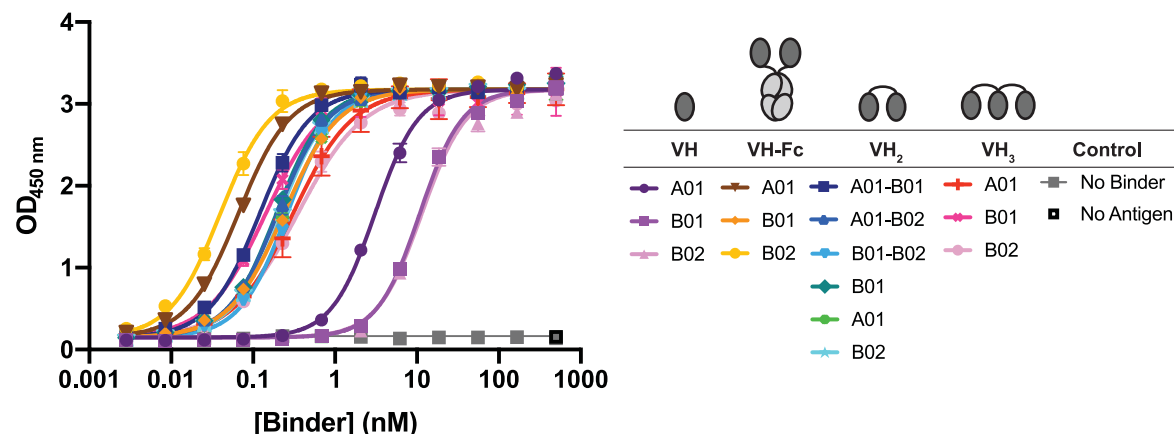
**Extended Data Fig. 1 | CDR loop design of VH-phage library.** Schematic of CDR amino acid composition as compared to parental template. Positions in pink highlight CDR H1 charged amino acid insertions. Positions in blue highlight the insertion of 'X' synthetic amino acid mixture. Positions in gray remain unchanged from template.



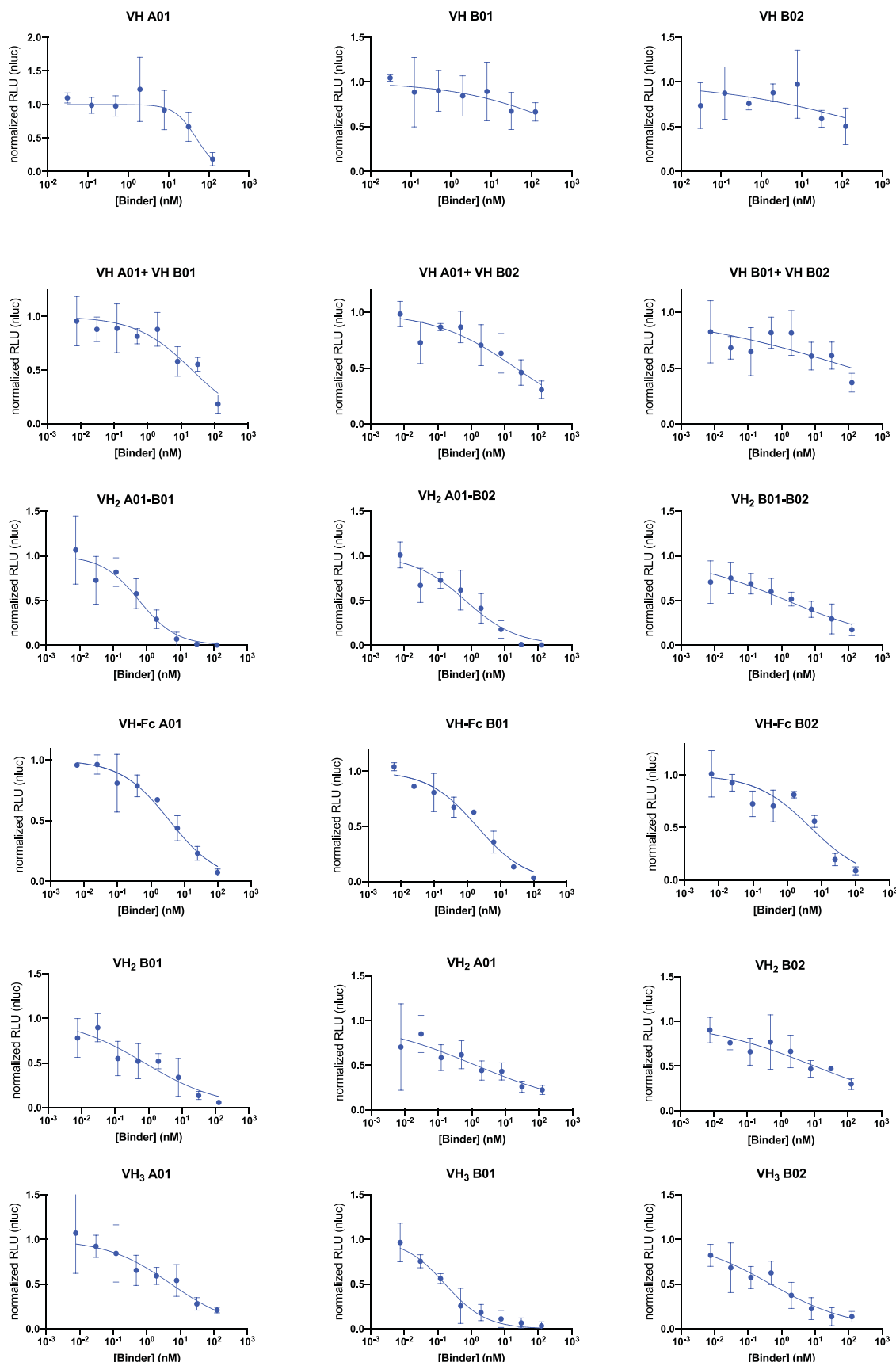
**Extended Data Fig. 2 | Specificity of lead VH domain binders.** Bio-layer interferometry (BLI) binding traces of VH domains at 150 nM to RBD and two decoy antigens expressed as biotinylated Fc-fusions: programmed cell death protein 1 (PD-1), and platelet glycoprotein 4 (CD36). Respective VH show successful binding to RBD, but not to either of the decoy antigens.



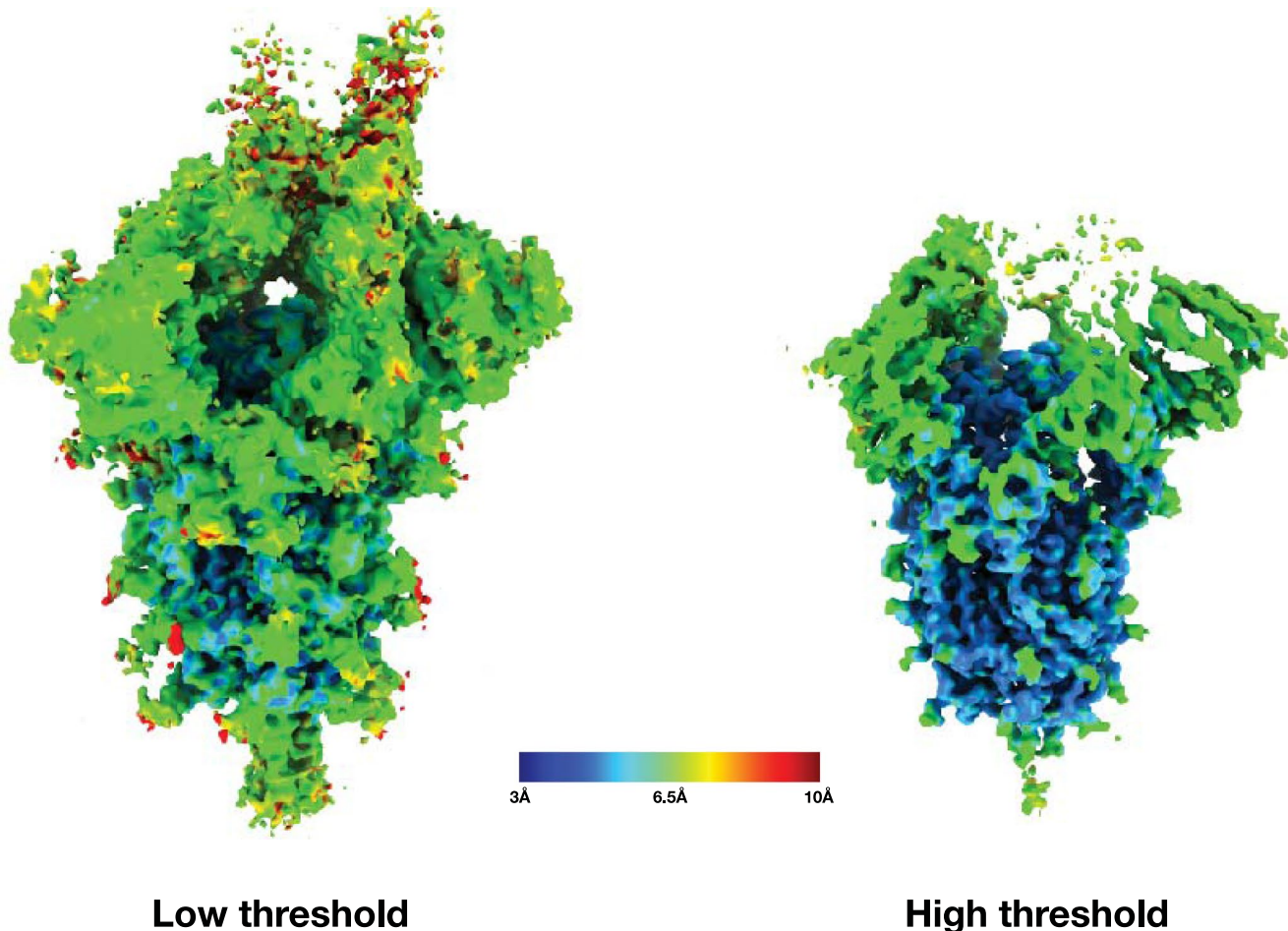
**Extended Data Fig. 3 | Measurements of inter-RBD distance on Spike trimer.** Structure of SARS-CoV-2 Spike trimer (PDB: 6VSB)<sup>32</sup>. RBD colored in blue is in the ‘up’ position while RBDs colored in green and pink are in the ‘down’ position. Distance between the mid-points of the ACE2 binding interface (PDB: 6M17)<sup>1</sup> on respective RBDs was measured in Pymol.



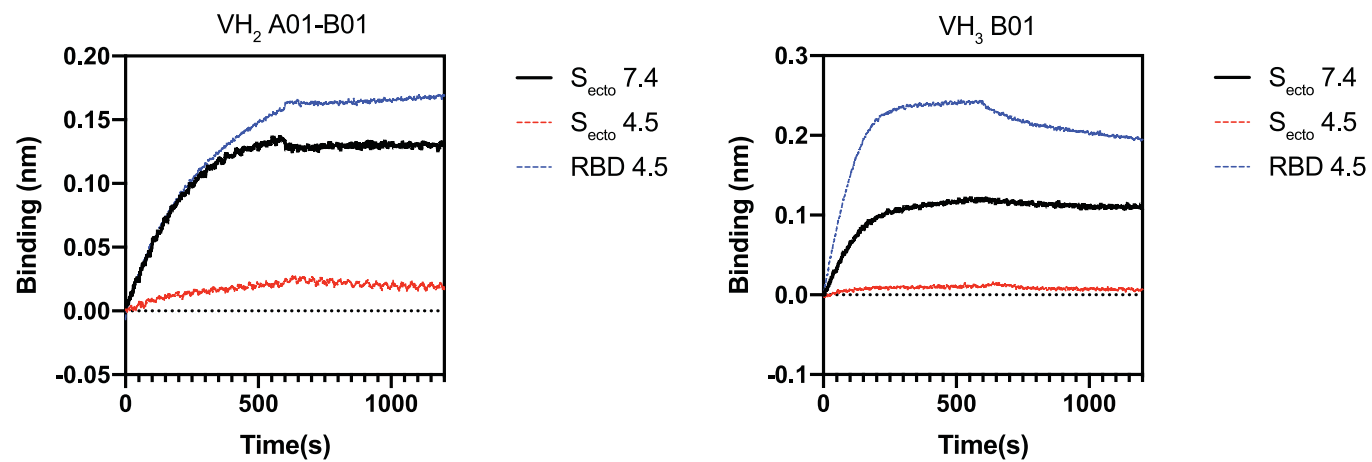
**Extended Data Fig. 4 | ELISA of VH binders to Spike-RBD.** ELISA of VH binders against Spike-RBD. Data presented show the average and standard deviation from three independent experiments. Data were fit to a non-linear, four-parameter variable slope regression model using Prism 8 to obtain EC<sub>50</sub> values for each binder.



**Extended Data Fig. 5 | Pseudotyped virus neutralization by VH Binders.** Pseudotyped virus neutralization assays of VH binders. Data represent average and standard deviation of two biological replicates. Data were fit to a non-linear, four-parameter variable slope regression model using Prism 8 to obtain IC50 values.



**Extended Data Fig. 6 | Cryo-EM reconstruction of SARS-CoV-2 Spike trimer.** The SARS-CoV-2 Spike trimer + VH3 B01 cryo-EM reconstruction from non-uniform refinement in cryoSPARC at two different thresholds colored by resolution in the range from 3 Å to 10 Å. At high threshold the core S2 clearly displays high resolution features but the periphery of the molecule is closer to 6–7 Å.



**Extended Data Fig. 7 | pH dependent binding of lead multivalent and bi-paratopic VH.** BLI assay of lead constructs at 25 nM to Secto and RBD at pH 7.4 or pH 4.5. Binding of VH leads is only observed with Secto at pH 7.4 and RBD at pH 4.5.

## Reporting Summary

Nature Research wishes to improve the reproducibility of the work that we publish. This form provides structure for consistency and transparency in reporting. For further information on Nature Research policies, see our [Editorial Policies](#) and the [Editorial Policy Checklist](#).

### Statistics

For all statistical analyses, confirm that the following items are present in the figure legend, table legend, main text, or Methods section.

n/a Confirmed

- The exact sample size ( $n$ ) for each experimental group/condition, given as a discrete number and unit of measurement
- A statement on whether measurements were taken from distinct samples or whether the same sample was measured repeatedly
- The statistical test(s) used AND whether they are one- or two-sided  
*Only common tests should be described solely by name; describe more complex techniques in the Methods section.*
- A description of all covariates tested
- A description of any assumptions or corrections, such as tests of normality and adjustment for multiple comparisons
- A full description of the statistical parameters including central tendency (e.g. means) or other basic estimates (e.g. regression coefficient) AND variation (e.g. standard deviation) or associated estimates of uncertainty (e.g. confidence intervals)
- For null hypothesis testing, the test statistic (e.g.  $F$ ,  $t$ ,  $r$ ) with confidence intervals, effect sizes, degrees of freedom and  $P$  value noted  
*Give P values as exact values whenever suitable.*
- For Bayesian analysis, information on the choice of priors and Markov chain Monte Carlo settings
- For hierarchical and complex designs, identification of the appropriate level for tests and full reporting of outcomes
- Estimates of effect sizes (e.g. Cohen's  $d$ , Pearson's  $r$ ), indicating how they were calculated

*Our web collection on [statistics for biologists](#) contains articles on many of the points above.*

### Software and code

Policy information about [availability of computer code](#)

Data collection Forte Bio Data Acquisition 12.0, Roche LC480 LightCycler Software 1.5.0, SerialEM 3.8

Data analysis Forte Bio Data Analysis 12.0, LightCycler Thermal Shift Analysis 2.0.2015.813, GraphPad Prism 8, ChimeraX 1.0, Rosetta 3.12, PyMOL v1.8.6.2, MotionCor2 v1.3, cyroSPARC v2.15.0. Next-generation sequencing (NGS) analysis was conducted using an in-house informatics pipeline written in R Version 1.2.5033, which has been deposited into GitHub: [https://github.com/crystaljie/VH\\_library\\_CDR\\_H3\\_NGS\\_analysis\\_Cole.Bracken.git](https://github.com/crystaljie/VH_library_CDR_H3_NGS_analysis_Cole.Bracken.git).

For manuscripts utilizing custom algorithms or software that are central to the research but not yet described in published literature, software must be made available to editors and reviewers. We strongly encourage code deposition in a community repository (e.g. GitHub). See the Nature Research [guidelines for submitting code & software](#) for further information.

### Data

Policy information about [availability of data](#)

All manuscripts must include a [data availability statement](#). This statement should provide the following information, where applicable:

- Accession codes, unique identifiers, or web links for publicly available datasets
- A list of figures that have associated raw data
- A description of any restrictions on data availability

Code used to analyze NGS data has been deposited onto Github and is available for download at: [https://github.com/crystaljie/VH\\_library\\_CDR\\_H3\\_NGS\\_analysis\\_Cole.Bracken.git](https://github.com/crystaljie/VH_library_CDR_H3_NGS_analysis_Cole.Bracken.git). Cryo-EM structural data have been deposited in the Protein Data Bank and Electron Microscopy Data Bank, (PDB 7JWB and EMD-22514). The cryo-EM structure of Spike trimer from PDB:6VSB and ACE2 from PDB: 6M17 and PDB:6M0J were used to for distance estimates. The cryo-EM structure of Spike trimer from PDB: 6X2B and crystal structure of a VH domain from PDB: 3P9W were used for cryo-EM data processing. Source data for Figures 1-4 and Extended Data Figures (2,4,5, and 7) are provided with this paper. Any additional information is available upon request.

# Field-specific reporting

Please select the one below that is the best fit for your research. If you are not sure, read the appropriate sections before making your selection.

Life sciences

Behavioural & social sciences  Ecological, evolutionary & environmental sciences

For a reference copy of the document with all sections, see [nature.com/documents/nr-reporting-summary-flat.pdf](https://nature.com/documents/nr-reporting-summary-flat.pdf)

## Life sciences study design

All studies must disclose on these points even when the disclosure is negative.

Sample size	Statistical methods to predetermine sample size were not conducted. Sample size of all data collected were chosen such that the interpretation of data were clear and fits to the data were good (chi-square test) or yielded statistical significance (p-value).
Data exclusions	No data were excluded from the analysis.
Replication	All quantitative measurements were obtained in biological replicates or triplicates, conducted on separate days. Additionally, within a biological replicate, two or three technical (within-assay) replicates were conducted. All attempts at replication were successful.
Randomization	Experimental study groups were not used in our study and thus randomization into such groups is not relevant to our study.
Blinding	Experimental groups were not used. Thus, blinding to group allocation was not conducted and is not relevant to our study.

## Reporting for specific materials, systems and methods

We require information from authors about some types of materials, experimental systems and methods used in many studies. Here, indicate whether each material, system or method listed is relevant to your study. If you are not sure if a list item applies to your research, read the appropriate section before selecting a response.

Materials & experimental systems		Methods	
n/a	Involved in the study	n/a	Involved in the study
<input type="checkbox"/>	<input checked="" type="checkbox"/> Antibodies	<input type="checkbox"/>	<input type="checkbox"/> ChIP-seq
<input type="checkbox"/>	<input checked="" type="checkbox"/> Eukaryotic cell lines	<input type="checkbox"/>	<input type="checkbox"/> Flow cytometry
<input checked="" type="checkbox"/>	<input type="checkbox"/> Palaeontology and archaeology	<input type="checkbox"/>	<input type="checkbox"/> MRI-based neuroimaging
<input checked="" type="checkbox"/>	<input type="checkbox"/> Animals and other organisms		
<input type="checkbox"/>	<input checked="" type="checkbox"/> Human research participants		
<input checked="" type="checkbox"/>	<input type="checkbox"/> Clinical data		
<input checked="" type="checkbox"/>	<input type="checkbox"/> Dual use research of concern		

## Antibodies

Antibodies used	VH A01, VH B01, VH B02 and anti-M13-HRP conjugate (Sino Biologicals, catalog # 11973-MM05T-H, lot #: 9547458)
Validation	VH A01, VH B01, VH B02 were derived from a in-house human single-domain variable-heavy (VH)-phage synthetic library. The construction and validation of the VH-phage library, in addition to the recombinant VH are provided in the study. In brief, the amino acid sequence of each recombinant human VH domain antibody described in this study was verified by Sanger sequencing of the plasmid encoding the VH domain antibody. Specificity and affinity for SARS-CoV-2 Spike RBD was confirmed by BLI (Figure 2, and Extended Data Fig. 2). anti-M13-HRP conjugate (Sino Biologicals, catalog # 11973-MM05T-H, lot #: 9547458): <a href="https://www.sinobiological.com/antibodies/m13-11973-mm05t-h">https://www.sinobiological.com/antibodies/m13-11973-mm05t-h</a>

## Eukaryotic cell lines

Policy information about <a href="#">cell lines</a>	
Cell line source(s)	HEK-ACE2 cells were a gift from A. Wiita's laboratory at UCSF and were generated by lentiviral transduction of HEK293T cells originally purchased from ATCC (CRL-3216). VeroE6 cells were a gift from Dr. J. DeRisi's laboratory at UCSF, and was originally purchased from ATCC (CRL-1586).
Authentication	Cell lines were confirmed by visual inspection. No further authentication was performed.
Mycoplasma contamination	Cell lines were tested negative for mycoplasma contamination.

Commonly misidentified lines  
(See [ICLAC](#) register)

No commonly misidentified cell lines were used in this study.

## Human research participants

Policy information about [studies involving human research participants](#)

### Population characteristics

COVID-19 convalescent patient sera were a kind gift of Dr. Michael Wilson (UCSF). Sera were obtained from patients with a historical positive nasopharyngeal SARS-CoV-2 RT-PCR test and were collected at least 14 days following the resolution of their symptoms. Healthy control serum was obtained prior to the emergence of SARS-CoV-2. As the goal of these studies was to assess how the convalescent SARS-CoV-2 antibody pool compared to our engineered constructs, the only relevant variable in this population was prior positive SARS-CoV-2 RT-PCR test. We do not anticipate gender, age, or co-morbidities to affect the conclusions drawn from experiments using these samples.

### Recruitment

Patients were voluntarily recruited based on their history of prior SARS-CoV-2 infection. All patients provided written consent. Patient sera were collected by the Wilson Lab and de-identified prior to delivery to the Wells Lab, where all experiments presented described here were performed. As patients were recruited exclusively on the basis of a prior positive SARS-CoV-2 RT-PCR test, we do not anticipate any self-selection bias or other biases to affect the results presented here.

### Ethics oversight

Patient sera were collected in accordance with the Declaration of Helsinki using protocols approved by the UCSF Institutional Review Board (Protocol 20-30338).

Note that full information on the approval of the study protocol must also be provided in the manuscript.